Master Thesis

Measurement of the local surface homogeneity of CBM RICH mirrors using the Ronchi method

Messung der lokalen Oberflächenhomogenität von CBM-RICH-Spiegeln mit dem Ronchi-Test

Cornelius Feier-Riesen

Dezember 2019

Justus-Liebig-Universität Gießen

Fachbereich 07: Mathematik und Informatik, Physik,
Geographie

Autor: Cornelius Feier-Riesen

Matrikelnummer: 5002383

Betreuung: Frau Prof. Dr. Claudia Höhne

Abgabe: Dezember 2019

Motivation

"All is number!"

This expression, as simplistic as it might appear, opens a deep insight into a mind that is vastly astonished about the order and principles of nature and its laws. In its intensity it might be much more profound than Archimedes *„Eureka!“*. It does not only reveal the amazement for a sole solved problem, but a great impression about being aware that all processes in nature can be calculated and are predictable[1].
The Greek philosopher Pythagoras of Samos (580-500 B.C.), to whom this expression is referred, apparently had been so amazed of the intelligibility of nature, that, according to some written records, he dedicated his life to mathematics and established a school to promote mathematical and philosophical thinking that is based on facts and logic. He taught that the harmony of the cosmos can be explained by proportions of numbers. In particular in music he noticed that the harmony of accords can be led back to numerical proportions of numbers, namely in the length of the strings of a string instrument. Unlike other philosophical approaches to explain the world, Pythagoras did not seek the explanation in a primordial matter, but in a primordial law that guides all procedures. [1]
But not only Pythagoras was amazed by the mathematical structure of nature, also many other philosophers and scientists were and still are amazed by the natures order. In his book *„The Meaning of it all“*, the ingenious thinker, physicist and Nobel prize winner Richard Feynman says:

> *„The fact that there are rules at all to be checked is a kind of miracle; that it is possible to find a rule, like the inverse square law of gravitation, is some sort of miracle.“*[2]

Eugene Wigner, another well known physicist and Nobel laureate as well, dedicated an article with the title *„The Unreasonable Effectiveness of Mathematics in Natural Sciences“* to this issue. And indeed, it *is* something to

---

[1] if all initial conditions are known; as we know at least since the upcoming of quantum mechanics, this is not completely true, but a good approximation in daily experience and also more complex problems

[2] see [2], page 34

wonder about. Is the comparatively simplistic inverse square law of gravitation able to amaze people, just think of the amazing symmetry in physics, described by group theory, or the ingenious and elegant solution of the quantum harmonic oscillator with the creation and annihilation operators $\hat{a}$ and $\hat{a}^{\dagger}$. *„If you are not confused by quantum physics then you haven't really understood it.“* was Niels Bohr's reaction.[3]
This mathematical structure in nature is used in physical experiments to explore dependencies of various quantities. The RICH detector, in whose scope this thesis is done, is responsible to investigate electromagnetic radiation that is emitted from heavy ion collisions. By the amount and properties of this radiation and by other observables the aim of the CBM experiment, to investigate the QCD phase diagram in a certain region, can be performed.

The theory part starts with the introduction of the Standard Model of particle physics. This chapter is followed by a chapter about scattering experiments. My motivation therefor was to let the reader know how one can conclude on the structure and properties of tiny particles from scattering experiments, which are, together with the underlying mathematics, the basis of high energy physics.

---

[3] see [3], preface, p. vii

Abstract

This thesis is about the development of a so called Ronchi test, invented by Vasco Ronchi. It had been developed to check spherical surfaces for their accuracy in curvature and, in this particular case, is used to test the mirrors for the Ring Imaging Cherenkov Detector (RICH), which is part of the Compressed Baryonic Matter (CBM) experiment at the future FAIR facility in Darmstadt. This experiment is still in preparation and will be established to explore a certain region of the phase diagram of Quantum Chromo Dynamics (QCD). Electromagnetic radiation from the dense fireball, created in heavy ion collisions, is one of the important probes to be investigated. With this measurement and other observables the aim is to characterize the matter being created.
The spherical RICH mirrors are built to focus the photons, that are produced by Cherenkov radiation from electrons and pions, traversing the RICH, onto a photo multiplier plane. The conically emitted photons are focussed as ring whose radius depends on the velocity of the particles. By knowing the particles energy and velocity, one can conclude on their mass and hence distinguish electrons from pions, which will be the main task of the RICH detector. Since only a few photons per ring (≈ 20) will be detected, it is of absolute necessity to display them with high accuracy onto the plane, so it is inevitable to have a good knowledge of the mirrors surface profile.

The developed Ronchi test setup allows to extract local information of the surface homogeneity of the mirror surface. The Ronchigrams directly give a qualitative information which e.g. shows a clear impact of the mirror holders that have been glued to the back side of the mirrors. In this regions the reflectivity seems to be strongly reduced. The main effort of this thesis was the implementation of a C++ routine to extract quantitative information on the deviation of the mirror surface from an ideal sphere. This routine has successfully been completed and first results are shown and discussed.

Zusammenfassung

Diese Thesis beschreibt den Aufbau des von Vasco Ronchi erfundenen Ronchitests. Dieses Verfahren wurde entwickelt, um die Krümmung sphärischer Oberflächen zu prüfen, hier speziell angewendet für die Spiegel des RICH-Detektors (Ring Imaging Cherenkov) des CBM-Experiments (Compressed Baryonic Matter) an der im Bau befindlichen FAIR-Anlage bei Darmstadt. Das CBM-Experiment befindet sich noch in der Entwicklungsphase und dient der Untersuchung eines bestimmten Bereichs des QCD-Phasendiagramms (Quantum Chromo Dynamic). In Schwerionenkollisionen wird heiße und dichte Kernmaterie erzeugt, bei deren experimenteller Untersuchung elektromagnetische Sonden eine besondere Rolle spielen. Ihre Messung im CBM-Experiment hat hohe Priorität. Aus diesen und anderen Indikatoren sollen die Eigenschaften der erzeugten Materie erforscht werden.
Durch den Cherenkoveffekt der Elektronen und Pionen, die den RICH-Detektor durchfliegen, entstehen Photonen. Diese werden kegelförmig ausgesandt und durch die sphärischen Spiegel auf die Photomultiplier-Ebene (PMT) fokussiert, wo sie als Ring erscheinen. Dabei ist der Ringradius abhängig von der Geschwindigkeit der Elektronen und Pionen. Sind Energie und Geschwindigkeit der Teilchen bekannt, können deren Masse bestimmt und Elektronen daher von Pionen unterschieden werden, was die Hauptaufgabe des RICH-Detektors sein wird. Da nur wenige Photonen pro Ring detektiert werden (ca. 20), ist es von größter Wichtigkeit, diese mit hoher Genauigkeit auf die PMT-Ebene abzubilden. Dieser Umstand erfordert eine genaue Kenntnis des Oberflächenprofils der Spiegel.

Der entwickelte Ronchitest-Aufbau erlaubt es, die lokale Oberflächenhomogenität zu untersuchen. Die Ronchigramme geben direkt qualitative Informationen über die Oberfläche, z.B. sieht man deutlich einen Einfluss der auf der Rückseite der Spiegel angeklebten Elemente zur Spiegelhalterung. In diesen Bereichen ist die Reflektion des Lichtes deutlich reduziert. Das wesentliche Ergebnis dieser Arbeit ist die Implementierung einer C++-Routine zur quantitativen Berechnung der Abweichungen der Spiegeloberfläche von der idealen Oberfläche. Die Routine wurde erfolgreich implementiert und erste Ergebnisse werden dargestellt und diskutiert.

Contents

1 Standard Model of Particle Physics

1.1 Introduction

The Standard Model of particle physics comprises the fundamental particles and their interactions among each other. The particles can be grouped into fermions (quarks and leptons), of which matter is built from, and bosons (e.g. the photon) that are the mediators of the strong, the weak or the electromagnetic force. These two types of particles differ in their spins. While fermions have an half-integrated spin, bosons spins are whole numbered. The type of spin a particle carries has a great impact on its so called occupancy number (number of particles in a certain (energy) state). Since for fermions the Pauli principle is valid, which forbids two fermions to be in exactly the same state (i.e. to agree in all quantum numbers), their accumulation behaviour differs enormously from that of bosons. No two fermions can have the same quantum numbers at the same place. Adding two fermions with different spin quantum number, i.e. $+\frac{1}{2}$ and $-\frac{1}{2}$, two fermions can be bound to form a boson with integer spin. There are six types of each, quarks and leptons, plus their antiparticles. Quarks and leptons each are subdivided into three „families“ or „generations“ with different masses, the first generations containing the lightest particles. All visible and stable matter is built from the two lightest quarks, (up and down quark) and the lightest charged lepton (electron). The heavier particles, once generated, promptly decay into the lighter and more stable ones. Their lifetimes are very small but range over many magnitudes of order. For example, the lifetime of a muon is $\tau_\mu = 2,2 \times 10^{-6}$ seconds, what counts to be quite long in the subatomic world, whereas the shortest measured lifetime is that of the Z^0 boson: $\tau_{\mathrm{Z}^0} = 3 \times 10^{-25}$ seconds.
The Standard Model has emerged since the 1960s, driven by both, experimental and theoretical progress. But even though the basic research of the subatomic world is quite advanced, there are still some issues left that are not explained by the Standard Model. So for instance many parameters (masses, coupling constants, CKM coefficients etc.) can not be derived from first principle but need to be measured. And also the most familiar force, the gravity, cannot be included into this model and thus won't be treated here.
Particles can decay into other particles. These processes are strictly obeying certain rules, like energy or charge conservation. Those two are conserved always, despite which interaction is taking place. Other quantities are conserved only by certain forces but not by all. Some of these processes and

rules will be briefly mentioned below, but it would go beyond the scope of this thesis to describe them all.

1.2 Fermions

1.2.1 Quarks

It had been mentioned above, that there are two types of fermions: quarks and leptons. At first we will have a look at the quarks and then see their differences to the leptons.
Quarks have spin $S_q = \frac{1}{2}$ and there are six different types of quarks that are called *flavors*: up (u), down (d), charm (c), strange (s), top (t) and bottom (b). They can be arranged into three generations with increasing mass (for more detailed values see Fig. 1.1):

$$\begin{pmatrix} u \\ d \end{pmatrix}, \begin{pmatrix} c \\ s \end{pmatrix}, \begin{pmatrix} t \\ b \end{pmatrix}.$$

Quarks are subject to the strong, the weak and the electromagnetic interactions and carry electric charge and color charge. While the quarks from the upper row have the electric charge number $z_q = +\frac{2}{3}$, the quarks from the lower row have $z_q = -\frac{1}{3}$, in units of the electric charge e. The color charge of a quark can be either red, green or blue. Antiquarks have versed electric and color charge, so for instance the antiup quark ($\bar{u}$) has $z_q = -\frac{2}{3}$ and can carry the color charge antired, antigreen or antiblue. Such as positive and negative electric charge are cancelling each other, color and anticolor do so as well. But not only color and anticolor are neutralizing each other, the three colors combined are also neutral or „white“, such as the three anticolors combined. Heavier quarks can decay into lighter quarks with participation of a charged boson ($W^{\pm}$, see next section). Since the boson is charged and charge has to be conserved, the final quark has to have a different charge than the initial one (because $z_{q1} = z_{q2} + z_{W^{\pm}}$). So for instance a charm quark cannot decay into an up quark. The decay of a quark with participation of the neutral Z^0 boson has not been observed yet and is subject of current research.
The probabilities for the transformation among the quarks are shown in the unitary Cabibbo-Kobayashi-Maskawa matrix (CKM), where V_{ij} means the transition probability between quarks i and j. The approximate values are:

$$\begin{pmatrix} V_{ud} & V_{us} & V_{ub} \\ V_{cd} & V_{cs} & V_{cb} \\ V_{td} & V_{ts} & V_{tb} \end{pmatrix} = \begin{pmatrix} 0.974 & 0.225 & 0.004 \\ 0.225 & 0.973 & 0.041 \\ 0.009 & 0.040 & 0.999 \end{pmatrix}.$$

A very important principle to know about is the *confinement* of quarks. In an environment with moderate temperatures and pressure, quarks are not free but are building bound states with other quarks. In those bound states the colors of the participants are always combining to „white“. So for example a system of two quarks, called meson, might contain a blue and an antiblue quark. Or a baryon, a system of three quarks, will contain quarks that carry red, green and blue color (or their anticolors). The reason for this phenomena is the binding potential V_{QCD} (QCD from „quantum chromo dynamics“) between two quarks:

$$V_{\mathrm{QCD}} = -\frac{4}{3}\frac{\alpha_s(r)\hbar c}{r} + kr. \tag{1.1}$$

For small distances r the potential has a large negative value, while at larger distances the linear term of the potential dominates. Thus one has to put a lot of energy into the system to increase the distance between two quarks. At a certain distance V_{QCD} would be so large that it costs less energy to create a new pair of a quark and an antiquark than further separating of the quarks. Therefore quarks never occur as free particles but are confined into hadrons.

1.2.2 Leptons

Such as the quarks, also leptons carry spin $S_l = \frac{1}{2}$ and can be sorted into three generations. But unlike the quarks only one member of a generation has an electrical charge, while the other one is neutral. The members of the first generation are the electron (e^-) and the electron neutrino (ν_e). The second and third generation contain the muon (μ^-) and the tau (τ^-) with their neutrino partners (ν_μ and ν_τ). The electron, muon and tau are negatively charged with $z_l = -1$ in units of the electron charge e, the neutrinos are neutral. These leptons also have antiparticles that are positively charged in case of the antielectron (e^+), antimuon (μ^+) and antitau (τ^+) and neutral in case of the antineutrinos. All leptons are subject to the weak interaction, the charged ones additionally to the electromagnetic interaction.

As mentioned, quarks can decay, following certain rules. In reactions with leptons, a new conservation law comes up, namely the conservation of the so called *lepton numbers* L_e, L_μ, L_τ. Electrons and electron neutrinos have the lepton family number $L_e = 1$, their antiparticles the lepton number $L_e = -1$. Analogously the family numbers of the muon and tau are calculated. The lepton number $L = L_e + L_\mu + L_\tau$ is conserved since the lepton family numbers are conserved separately. See for instance a muon decayings into an electron:

$$\mu^- \rightarrow e^- + \bar{\nu_e} + \nu_\mu.$$

The initial state has the lepton number $L = L_\mu = 1$. Thus, the final state has to have the lepton number $L = L_\mu = 1$ as well. Hence, further decay products are necessary to conserve L_e and L_μ. Those are found to be neutrinos.

1.3 Bosons and Fundamental Interactions

1.3.1 Photons, $W^\pm$ and Z^0 and the Electro Weak Unification

Photons, $W^\pm$ and Z^0 bosons have the spin $S = 1$. While the photon, or γ, is massless and mediates the electromagnetic interaction, the $W^\pm$ and Z^0 bosons are very massive with masses of 80 GeV ($W^\pm$) and 91 GeV (Z^0), respectively, and are responsible for the weak interaction. As indicated, the Z^0 is neutral and the $W^\pm$ carry positive or negative electric charge with the charge number $z_W = \pm 1$. In collider experiments at energies large enough, they can be created by annihilation of a lepton-antilepton or quark-antiquark pair. Due to charge conservation the $W^\pm$ are created in W^+ W^- pairs (f stands for „fermion“):

$$f^+f^- \rightarrow \gamma, \qquad f^+f^- \rightarrow Z^0, \qquad f^+f^- \rightarrow W^+ + W^-.$$

The larger the mass of the final product, the larger the energy of the initial particles has to be. Such experiments can be performed at large accelerator labs such as CERN, where the Z^0 and $W^\pm$ bosons have experimentally been detected for the first time in 1983.

The range of the electric and weak interaction are largely different from each other. Since the photon is massless, its range is infinite. On the contrary, the massive Z^0 and $W^\pm$ bosons reach only very short distances. Further, the two interactions are mediated with different strengths, i.e. *coupling constants* (at closer examination these constants are not really constant but dependent on the momentum transfer in a reaction). The electromagnetic coupling constant α_{em} is

$$\alpha_{\text{em}} = \frac{e^2}{4\pi\epsilon_0\hbar c} \approx \frac{1}{137}. \tag{1.2}$$

In the sixties of the last century, S. Glashow, S. Weinberg and A. Salam proposed the electroweak theory with which two of the fundamental forces, the weak and the electromagnetic force, could be united. The electromagnetic and weak coupling constants can then be expressed in terms of the electroweak coupling constants g and g'. The photon and Z^0 boson are expressed as mixings of two different, fundamental states which add a neutral partner to the $\mathrm{W}^\pm$ bosons. This had been enabled by introducing a new quantum number, called *weak isospin*, postulating basic states $|\mathrm{B}^0\rangle$ and $|\mathrm{W}^0\rangle$, and expressing the detectable neutral bosons as linear combinations of these states:

$$|\gamma\rangle = \cos\theta_W |\mathrm{B}^0\rangle + \sin\theta_W |\mathrm{W}^0\rangle \tag{1.3}$$

$$|\mathrm{Z}^0\rangle = -\sin\theta_W |\mathrm{B}^0\rangle + \cos\theta_W |\mathrm{W}^0\rangle. \tag{1.4}$$

The angle θ_W is the so called *Weinberg angle* and defines the mixing. It can be determined in different ways, for example from electron neutrino scattering, the Z^0 width or by the mass ratio of $\mathrm{W}^\pm$ and Z^0. Its value had been calculated to be

$$\sin^2\theta_W = 0.23116 \pm 0.00012. \tag{1.5}$$

The Weinberg angle can be expressed in dependence of the coupling constants of the electroweak interaction:

$$\sin\theta_W = \frac{g'}{\sqrt{g^2 + g'^2}}, \quad \cos\theta_W = \frac{g}{\sqrt{g^2 + g'^2}}. \tag{1.6}$$

Finally the electric charge can be written in terms of g:

$$e = g \cdot \sin\theta_W. \tag{1.7}$$

1.3.2 Gluons

Gluons are the carriers of the strong interaction and bind the quarks in hadrons. They are not color neutral but carry a combination of color and anticolor. From group theory arises that there are 8 different gluons with the following possible combinations of colors:

$$\mathrm{r\bar{g}}, \quad \mathrm{r\bar{b}}, \quad \mathrm{g\bar{b}}, \quad \mathrm{g\bar{r}}, \quad \mathrm{b\bar{r}}, \quad \mathrm{b\bar{g}}, \quad \sqrt{\frac{1}{2}}(\mathrm{r\bar{r}} - \mathrm{g\bar{g}}), \quad \sqrt{\frac{1}{6}}(\mathrm{r\bar{r}} + \mathrm{g\bar{g}} - 2\mathrm{b\bar{b}}).$$

Since the gluons are carrying color charge, they are interacting among themselves and hence reduce the range of interaction to very small scales. From the first order calculations of perturbation theory the strong coupling constant α_s can be calculated as follows:

$$\alpha_s(Q^2) = \frac{12\pi}{(33 - 2n_q) \cdot \ln(Q^2/\Lambda^2)}. \tag{1.8}$$

Here n_q is the number of involved quarks. Λ is the so called cut-off parameter that has to be determined by experimental data ($\Lambda^2 \approx 0.06(\mathrm{GeV}/c)^2$), and $Q^2 = -q^2 = -(p - p')^2$, where p and p' are the four momentum vectors of the investigated particle before and after the reaction. A typical value for the strong coupling constant is $\alpha_s = 0.15$ (for $Q^2 \approx 3\,(\mathrm{GeV}/c)^2$ and two involved quarks).

As the electromagnetic and the weak interaction had successfully been unified, there are attempts to include the strong force as well into this model. This *Grand Unifying Theory* (GUT) would unify the interactions at very high energies of 10^{16} GeV.

1.3.3 Higgs Boson

The Higgs boson H is responsible for giving masses to the particles. It received its name from Peter Higgs, who, amongst others, postulated a new boson in 1964 to save the gauge invariance despite the existence of the massive exchange particles Z^0 and $\mathrm{W}^{\pm}$. Following the theory, the Higgs should have spin $S_H = 0$, thus being the only fundamental scalar boson. In summer 2012, discovery was claimed at CERN of the predicted Higgs boson with a mass of 125 GeV.

1.4 Hadrons

Hadrons are bound states of the srong interaction and most prominently can be divided into mesons ($\mathrm{q\bar{q}}$) and baryons (qqq). The well known protons and neutrons are the lightest baryons ($m_{p/n} \approx 940$ MeV) and are built up from two up and one down quark (uud) and one up and two down quarks (udd), respectively. The lightest mesons are pions ($m_\pi \approx 140$ MeV) which are made up from the up and down quarks and their antiparticles. Since quarks have half numbered spin, mesons are bosons whereas baryons are fermions.

Since long, exotic hadrons were predicted, consisting of more than three quarks or gluons. Only recently first particles could be detected that unambiguously do have an exotic substructure. In 2008 the Belle experiment in

Japan could at first prove the existence of a so called *exotic hadron*, i.e. a hadron that consists of more than three quarks.
[4, 5, 7, 8, 9, 10, 12]

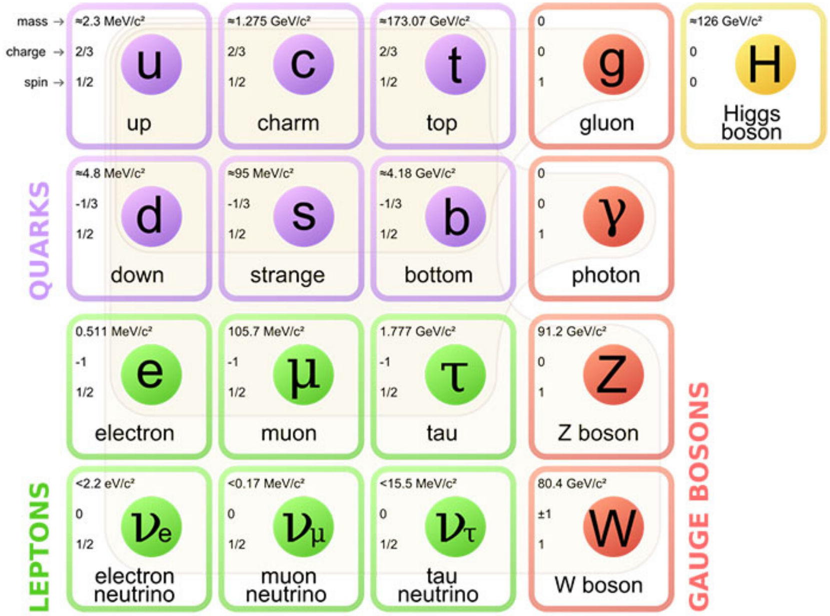

Figure 1.1: An overview of the fundamental fermions and bosons (without their antiparticles) with their masses, charges and spins. The neutrinos in the bottom row are underlying the weak force. The charged leptons underlie the weak and the electromagnetic force whereas the quarks are subject to the weak, the electromagnetic and the strong force. [11]

2 Scattering Experiments and Form Factors

2.1 Introduction

Since ancient times people were wondering about how matter is constructed and some assumed that all being could be reduced to several few basic elements.

The Standard Model of Particle Physics describes what matter is constructed from and how these smallest particles are interacting with each other. One of the most important tools to measure the structure of atoms were the first scattering experiments and a good understanding of the underlying physics and mathematics, respectively. At these experiments a particle beam with known energy is channeled onto a target and by the number and scattering angle of deflected particles one can extract the (sub)atomic structure of the target.

The first pioneering scattering experiment was the Rutherford scattering experiment in 1909, at which Hans W. Geiger and Ernest Marsden, two assistants of Ernest Rutherford, let alpha particles impinge on a gold foil. The result was surprising, since not all alpha particles traversed the gold foil, as expected, but a part of them (10^{-4}) had been reflected, some even by 180°. This led in 1911 to the Rutherford Model where the atom had a positively charged nucleus that was very small in relation to the whole atom, and electrons that were presumed to orbit the core and forming the atom shell. Until then Thomsons plum pudding model was the conception of the atom, where the negative electrons were considered to be in between a uniform cloud of positive charges.

The question is how one can deduce on the structure of the target from the scattered particles. To be able to answer this question a good knowledge of scattering theory is required. Rutherford defined a measurable quantity for the probability of deflections into a certain solid angle (see next section) and compared it with expressions derived from quantum mechanics, such as Fermis golden rule. After some mathematical transformation one ends up at a certain expression, called form factor, which contains all information about the spatial charge distribution of the target. The first models were rough but good approximations that neglected the influences of back scattering of the target, spin, and relativistic and quantum mechanical effects. These approximations had been improved later by Rutherford himself as well as by Nevill F. Mott, by including the mentioned effects step by step into the model.

A short overview on how one can get information about the structure of atomic particles from the results of scattering experiments is given below.

2.2 From Scattering Experiments to Form Factors

The differential cross sections $\frac{\mathrm{d}\sigma}{\mathrm{d}\Omega}$ gives the probability of a particle to be deflected by the angle ϑ into a certain solid angle unit $\mathrm{d}\Omega = 2\pi \sin\vartheta \, \mathrm{d}\vartheta$ and can be determined experimentally. The Rutherford differential cross section can be expressed as

$$\left(\frac{\mathrm{d}\sigma}{\mathrm{d}\Omega}\right)_{Rutherford} = \frac{(Ze^2)^2}{(4\pi\epsilon_0)^2 \, 4E^2 \sin^4 \frac{\vartheta}{2}}. \tag{2.1}$$

Here Ze means the charge of the target nucleus, E the energy of the particle beam and ϵ_0 the vacuum permittivity. As mentioned above, in this expression the back scattering of the target atom, the spins and relativistic and quantum mechanic effects are neglected and had been considered later. From Fermis golden rule

$$R = \frac{2\pi}{\hbar} |\langle\psi_f|\mathcal{H}|\psi_i\rangle|^2 \frac{\mathrm{d}n}{\mathrm{d}E'}, \tag{2.2}$$

which is the reaction rate per target particle and incident particle, and knowing that this rate is equal with the product of the total cross section and the velocity of the incident particles, divided by the scale volume, so $R = \frac{\sigma v}{V}$, another expression for the differential cross section can be obtained:

$$\frac{\mathrm{d}\sigma}{\mathrm{d}\Omega} = \frac{V^2 E'^2}{(2\pi)^2 (\hbar c)^4} |\langle\psi_f|\mathcal{H}|\psi_i\rangle|^2. \tag{2.3}$$

Here the velocity v had been approximated with the velocity of light c. The expression in the brackets is the matrix element and gives the probability for the transition of a particle from the initial state i into the final state f and the ψ_l are their wave functions, while $\mathcal{H}$ is the Hamiltonian of the system. Making use of the Born approximation these wave functions can be described by plane waves:

$$\psi_l = \frac{1}{\sqrt{V}} \mathrm{e}^{i\boldsymbol{p}_l \boldsymbol{r}/\hbar}. \tag{2.4}$$

In the present case, where charged particles are being scattered by other charged particles, the Hamiltonian is $\mathcal{H} = e\phi$. Thus, the matrix element can be written as

$$\langle\psi_f|\mathcal{H}|\psi_i\rangle = \frac{e}{V}\int \mathrm{e}^{-i\boldsymbol{p_f r}/\hbar}\phi(\boldsymbol{r})\,\mathrm{e}^{i\boldsymbol{p_i r}/\hbar}. \tag{2.5}$$

If the momentum transfer $\boldsymbol{q}$ is defined as $\boldsymbol{q} = \boldsymbol{p_i} - \boldsymbol{p_f}$, the matrix element can be transformed to

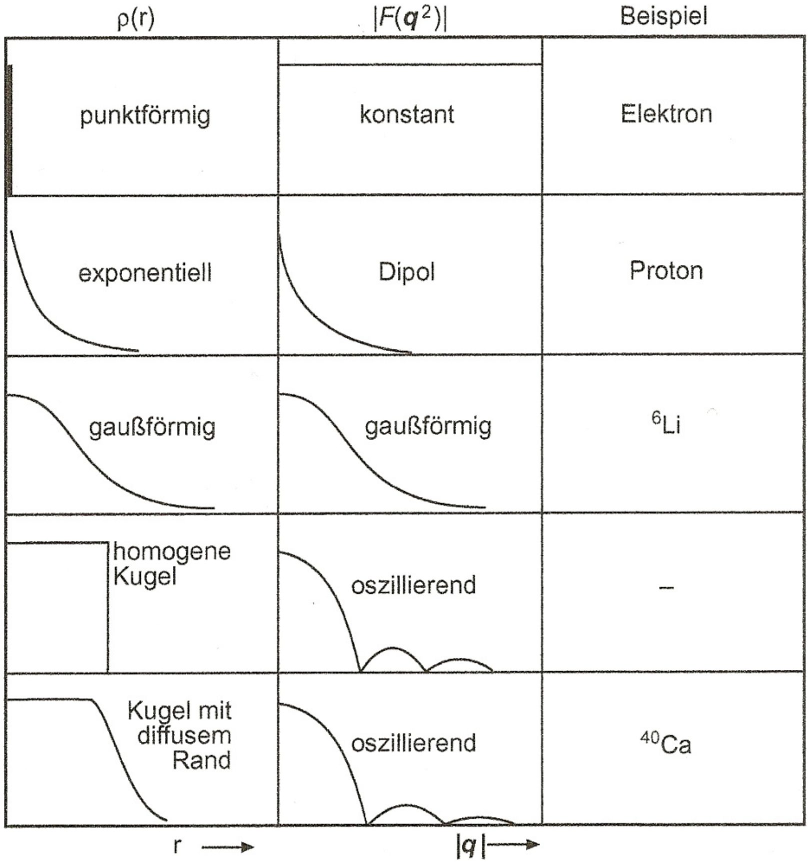

Figure 2.1: Different charge distributions $\rho(r)$ with their corresponding form factor curves $|F(\boldsymbol{q}^2)|$. [4]

$$\langle\psi_f|\mathcal{H}|\psi_i\rangle = \frac{e}{V}\int \phi(\boldsymbol{r})\,\mathrm{e}^{i\boldsymbol{qr}/\hbar}. \tag{2.6}$$

Using the Greens theorem, the Poisson equation $\Delta\phi = \frac{-\rho(\boldsymbol{r})}{\epsilon_0}$ and the charge distribution of a spherically symmetric system ($\rho(r) = Zef(r)$) the matrix element can finally be expressed as

$$\langle\psi_f|\mathcal{H}|\psi_i\rangle = \frac{4\pi\alpha\hbar^3 cZ}{|\boldsymbol{q}|^2 V}\int \mathrm{e}^{i\boldsymbol{qr}/\hbar} f(r)\mathrm{d}^3 r. \tag{2.7}$$

The integral

$$F(\boldsymbol{q}) := \int \mathrm{e}^{i\boldsymbol{qr}/\hbar} f(r)\mathrm{d}^3 r \tag{2.8}$$

is the already mentioned form factor of the charge distribution $f(r)$ and represents its Fourier transformation. All information about the spatial charge distribution of the target is contained in this expression. A list of several form factors with the corresponding charge distributions is given in table 2.1. A visualization of different charge distributions with examples can be seen in figure 2.1. [4]

shape	form factor $F(\boldsymbol{q^2})$	charge distribution $f(r)$	shape
constant	1	$\delta(r)/4\pi$	point
dipole	$(1+\boldsymbol{q^2}/a^2\hbar^2)^{-2}$	$(a^3/8\pi)\,\mathrm{e}^{-ar}$	exponentially
Gaussian	$\mathrm{e}^{-\boldsymbol{q^2}/2a^2\hbar^2}$	$(a^2/2\pi)^{3/2}\,\mathrm{e}^{-a^2r^2/2}$	Gaussian
oscillating	$3\alpha^{-3}(\sin\alpha - \alpha\cos\alpha)$	$\begin{cases} C & r \le R \\ 0 & r > R \end{cases}$	hom. sphere

Table 2.1: List of form factors with corresponding charge distributions (with $\alpha = |\boldsymbol{q}|R/\hbar$ and C a constant). [4].

In practice, a theoretical $F(\boldsymbol{q}^2)$ will be proposed and varied with diverse parameters until the best fit with the measured data is found. In figure 2.2, one of the first measurements of the form factor is presented. It shows the experimental data of the differential cross section $\frac{\mathrm{d}\sigma}{\mathrm{d}\Omega}$ of ^{12}C in dependence on the scattering angle ϑ together with a well fitted $F(\boldsymbol{q}^2)$. [4 - 6]

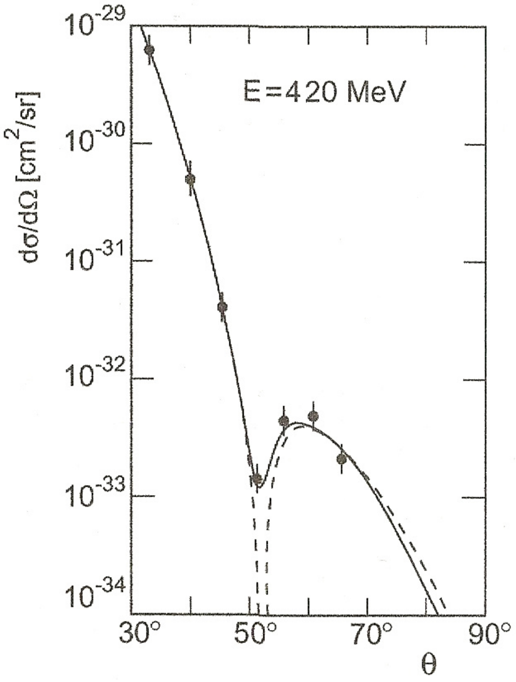

Figure 2.2: The cross section of ^{12}C, measured with a 420 MeV electron beam at 7 different angles (see the dots). The solid line corresponds to a fitted $F(\boldsymbol{q}^2)$ curve, the dashed line indicates the result for a plane wave, scattered at a homogeneous sphere with a diffuse edge. [4]

3 The QCD Phase Diagram

3.1 The Quark Gluon Plasma

As discussed, quarks are bound strongly into hadrons to form color neutral objects. This is valid for „moderate“ temperatures and pressures (concerning QCD, the temperatures within the sun are still moderate). From QCD simulations it had been calculated that at very high temperatures, such as approximately 150 MeV (which corresponds to 10^{12} Kelvin), the confinement is lifted and the hadronic matter turns into a state called *quark gluon plasma*. In the first microseconds after the big bang, the temperatures and densities were high enough to form such a state. Still, in neutron stars at low temperatures, the density is sufficient to provide the existence of a quark gluon plasma.

The number of hadron species, measured by high energy experiments, is increasing exponentially with the hadron mass. By QCD thermodynamic models an upper temperature limit T_c for the increase of hadronic matter can be calculated with use of the *bag model* (see Fig. 3.1). In this model the hadrons are considered to be bags of perturbative vacuum with a certain pressure or energy density E_{bag}, surrounded by normal vacuum with the energy density E_{vac}. A bag constant B is defined to be $B = E_{bag} - E_{vac}$. In the model of an ideal gas, consisting of massless pions, the pressure is given by

$$P_{\mathrm{id}} = 3\frac{\pi^2}{90}T^4. \tag{3.1}$$

The factor 3 considers the three possible charge states (-1, 0, +1) of the pion. For the quark gluon plasma, an equivalent expression can be obtained:

$$P_{QGP} = \left(2 \times 8 + \frac{7}{8}(3 \times 2 \times 2 \times 2)\right)\frac{\pi^2}{90}T^4 - B = 37\frac{\pi^2}{90}T^4 - B. \tag{3.2}$$

The first term (2×8) respects the two spin states and eight color degrees of freedom of the gluons. The factors of the second term are due to the three color, two flavor, two spin and two particle-antiparticle degrees of freedom of the quarks, where $\frac{7}{8}$ is a correction value to get the correct statistics. From thermodynamics it is known that a system tries to get the state of lowest free energy and thus the highest possible pressure. Solving equation 3.2 with 3.1, the following expression is obtained for the critical temperature T_c:

$$T_c = \left(\frac{45}{17\pi^2}\right)^{\frac{1}{4}} B^{\frac{1}{4}} \tag{3.3}$$

The bag constant had been calculated from hadron spectroscopy and is

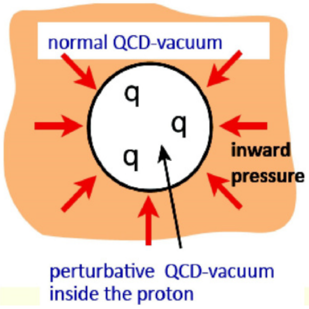

Figure 3.1: Bag model: the vaccum is considered to be „normal“ QCD vacuum, the bag (hadron) is treated as perturbative QCD vacuum. [15]

$B^{\frac{1}{4}} \approx 0.2$ GeV, resulting in $T_c \approx 150$ MeV. Though this bag model is built on a simplified principle, its quantitative predictions are quite close to more complex calculations. Values between 140 and 190 MeV had been calculated

for T_c. Recent calculations give $T_c \approx 155$ Mev with an error margin below 10 MeV [16]. The calculated results for T_c can vary, since they are dependent on which particle masses had been taken as scaling factor.
But not only high temperatures are dissolving this gaseous state of the hadrons. It is assumed that, at high densities and low temperatures, the hadrons are dissolving into their constituents, quarks and gluons, and form a color superconductor. This state had been studied less than the quark gluon plasma, since conventional algorithms break down at this point and new calculation methods are to be developed [16].

The dependence of the hadron states on temperature and net baryon density (or baryon chemical potential μ_B) is depicted in the QCD phase diagram in Fig. 3.2. Similar to the phase diagram of water it shows the different (assumed) states in dependence on temperature and density. However, much of the QCD phase diagram is still speculative, since „after decades of theoretical and experimental exploration, the sketch of the QCD phase diagram [...] is largely driven by (more or less well-grounded) speculation“ [16, p. 5].

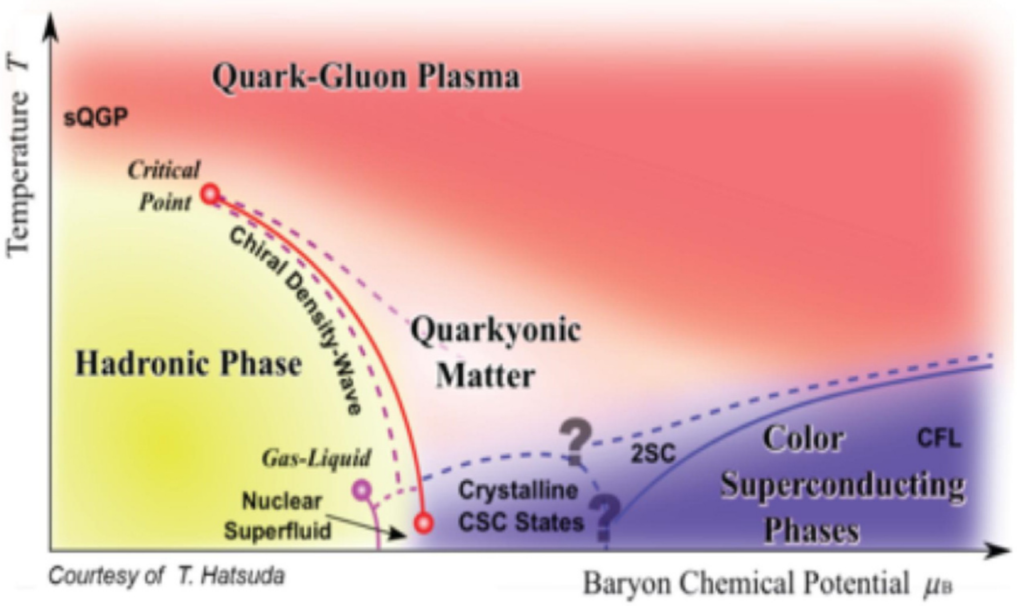

Figure 3.2: Phase diagram of the QCD. [13]

So, for instance, it is not yet known if the shown critical endpoint exists or not. Its existence would vastly help to understand the underlying physics of the phase diagram. An important argument for its existence is that an analytic cross-over at finite temperatures and zero baryon chemical potential has been proven, and it can be assumed from theory that at zero temperature and finite baryon chemical potential there is a chiral phase transition of first order, thus a critical point has to exist in between.
[13 - 16]

3.2 Experimental Investigation of the QCD Phase Diagram with Heavy Ion Collisions

The QCD phase diagram, as depicted in Fig. 3.2, can be investigated experimentally by means of heavy ion collisions. To investigate hadronic matter under these extreme conditions, one has to create systems at high temperatures and densities. This is done by accelerating heavy ions to high energies and let them collide (see Fig. 3.3). For a very short time, in the center of the collisions, very high temperatures and/or densities are given. The question now is how these quantities and properties can be determined. The methods one can use to study the unknown matter are for example hadronic and electromagnetic radiation, dissociation of passing quarkonium beams and the energy loss of passing hard jets [14, page 15].

Let us at first have a look at one possibility on how the *temperature* can be determined: The dissociation of quarkonia, bound states of either a bottom or charm quark with its antiparticle, can be taken as an indicator for the temperature. The binding energies of the ground states, J/ψ and Υ, are 0.6 GeV and 1.2 GeV, respectively, and are quite large in comparison to hadronic scales (see section 1.3.2, where $\Lambda^2 \approx 0.06$). This leads to small meson radii of 0.1 and 0.2 fm, respectively. As a consequence they can survive at temperatures above T_c. The binding energy decreases at higher excited quarkonium states, hence they are „melting“ at lower temperatures. Thus, by observing which particles are still leaving the hot and dense collision spot, one can conclude which temperatures had been there. In Fig. 3.4 a sketch is shown on how to estimate temperatures in dependence on the survival of the various charmonium states J/ψ, χ_c and ψ'.

The *energy density* can for example be tested by the energy loss of an energetic color charged particle. If the transition to deconfinement takes place,

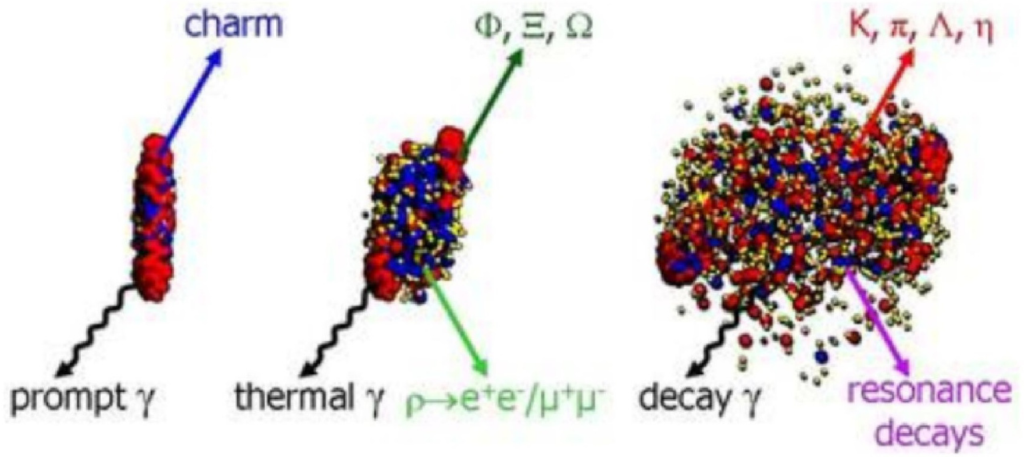

Figure 3.3: Sequences of a typical heavy ion collision (here: uranium ions at 23 AGeV energy): Collision of the length contracted ions (left), pre-hadronic phase of high density (middle), "freeze-out" phase, when all hadrons have been formed (right). The different colors indicate different particle types: projectile and target nucleons (red), excited baryons (blue), mesons (yellow). Such a collision evokes almost 1000 charged particles. [13]

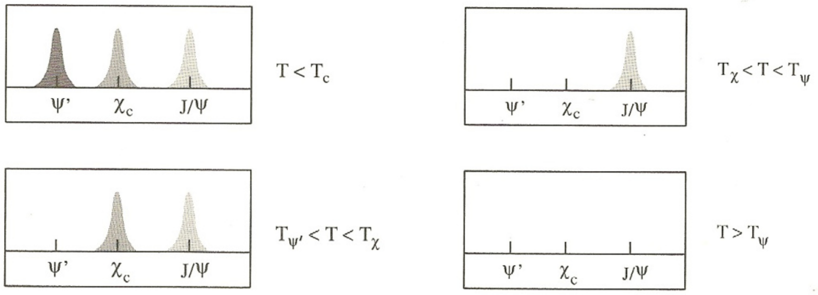

Figure 3.4: Sketch of various charmonium states, taken as thermometer. From the survival of the different excited states the temperature of the investigated medium can be estimated. [14]

the density increases by an order of magnitude and thus leads to a large energy loss of the probe particle. From calculations, it is assumed that the density in the interior of the fireball in high energy heavy ion collisions rises above 8 times the density of a nucleus (which already is more than 300 million tons per cm^3)(see Fig. 3.5). Since photons and dileptons (e^+e^- or $\mu^+\mu^-$

pairs), that had been produced by annihilation of a quark and an antiquark or by interaction of quarks or gluons, are interacting only electromagnetically, they leave the medium without further modification and can be used as a direct probe of the medium. To study the properties of the quark gluon plasma it is of importance to identify *electromagnetic radiation* that comes from the interior of the medium and thus from the hot and dense area.
The study of *hadronic radiation* is important to get information of early pre-hadronic stages and of the overall evolution of the system. In peripheral heavy ion collisions a non isotropic gradient in pressure causes a directed or an elliptic flow. From analysis of these forms of flow, conclusions can be made about the pressure in the fireball, but also on the formation of pre-hadronic states.
[13, 14, 17]

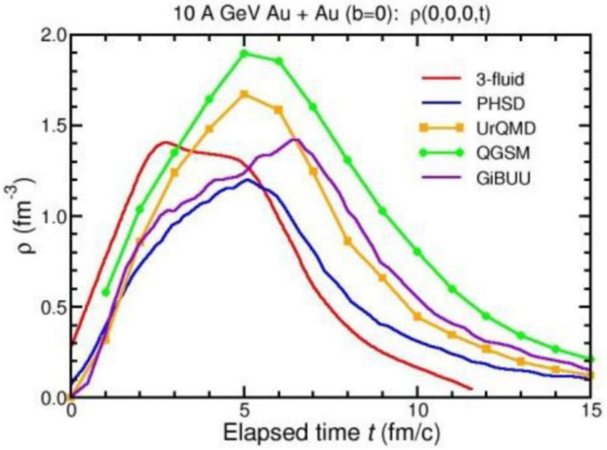

Figure 3.5: Density vs. time in the center of central Au+Au collisions, calculated by different models. The density $\rho = 1\ \text{fm}^{-3}$ is conform to the sevenfold density of a nucleus. [17]

4 The CBM Experiment

4.1 Detectors in general

The subatomic particles (quarks, leptons, hadrons) are differing in their masses and charges. So, to identify a particle, detectors have to be constructed that enable the measurement of its mass and charge. The sign of the charge can easily be determined by the direction of deflection in a magnetic field, whereas to determine the mass, one has to combine various types of measurements. In addition, the momentum has to be known in order to construct the particle energy.
The first detectors were small and could be placed on a desk. Some of them could only indicate that particles were there, as the blackened photographic plate of Henri Becquerel, detecting X-rays. Others, like the bubble chamber, were able to give the ratio of mass and charge by the radius of curvature of the particles trajectory due to the Lorentz force in the magnetic field. Later, when particles with higher energy were detected and the requirements for accuracy increased, the size of the detectors became immensely larger. The currently largest particle detector is the ATLAS detector at CERN.
The basic principle used to detect particles, is their energy loss in a medium, for instance by ionisation or by bremsstrahlung. The energy loss of a particle is described by the Bethe-Bloch formula:

$$-\frac{\mathrm{d}E}{\mathrm{d}x} = \frac{4\pi}{m_e c^2}\frac{nz^2}{\beta^2}\left(\frac{e^2}{4\pi\varepsilon_0}\right)^2 \cdot \left[\ln\frac{2m_e c^2\beta^2}{I(1-\beta^2)} - \beta^2\right]. \tag{4.1}$$

Here $\beta = \frac{v}{c}$ is the ratio of the particles velocity and velocity of light in vacuum, I the mean excitation potential of the atoms ($I \approx 16$ eV $\cdot Z^{0.9}$) and n the electron density. The total energy loss of a charged particle is composed of ionisation energy loss (Bethe-Bloch), bremsstrahlung, Cherenkov radiation, elastic scattering at the nuclei and nuclear reactions. Neutral hadrons can be detected via elastic scattering ($E \leq$ MeV), nuclear reactions (MeV $< E <$ GeV) and hadronic showers ($E >$ GeV), depending on their energy. So, for different particles with different energies, various detection principles had been invented. Therefore, complex particle detectors like ATLAS, built for the analysis of (nearly) all particles from a collision, do not contain only one detection principle but many. Thus becoming able to detect as many as possible different particles that had been created during the reaction. These sub detectors are arranged either in an onion skin principle around the colli-

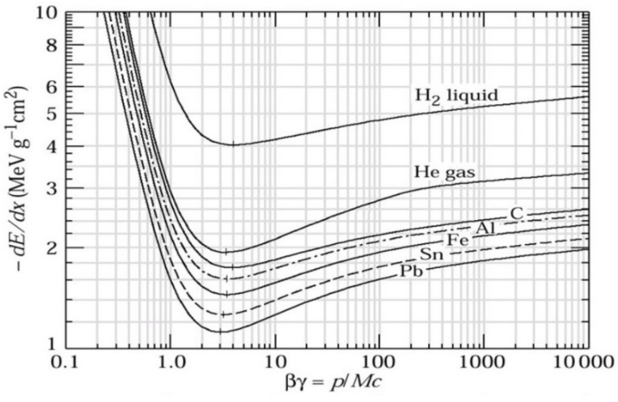

Figure 4.1: Energy loss per path length $-\frac{\mathrm{d}E}{\mathrm{d}x}$ in dependence on the particles momentum $\beta\gamma$, $\gamma = \frac{1}{\sqrt{1-\beta^2}}$. Momentum values shown are valid for a proton. For muons and pions the momentum scale has to be shifted by approximately one order of magnitude to smaller values. [7]

sion point in case of collisions at a collider, or in so called „forward direction“ in case of a fixed target experiment (see the CBM detector below). A few principles on how to measure particles with such a concept will be discussed briefly in the following.

The *energy* of a particle is measured by its energy loss in matter. Therefor the particle has to be absorbed completely by the detector material. By the amount of radiation during the absorption process one can conclude on the initial energy, since the yield of photons is proportional to the initial energy. This principle is called *calorimetry.* Depending on whether it is a charged lepton or a hadron, the calorimeters differ in their structure:

Electromagnetic calorimeters for low energies consist basically of a scintillator material (like sodium iodide) and photomultipliers (PMTs). For higher energies the principle of hadronic calorimeters is used (see below). Electromagnetic calorimeters measure the energy of photon or electron processes like bremsstrahlung and pair production that take place in the scintillator material. This is done by detecting the photons, that are emitted by the mentioned processes, with photomultipliers (PMTs). Their amount lets conclude on the initial energy.

Since hadrons have a very small reaction rate in scintillator material, *hadronic calorimeters* additionally consist of an absorber material, e.g. lead or uranium. These calorimeters are arranged in alternating layers of scintillating

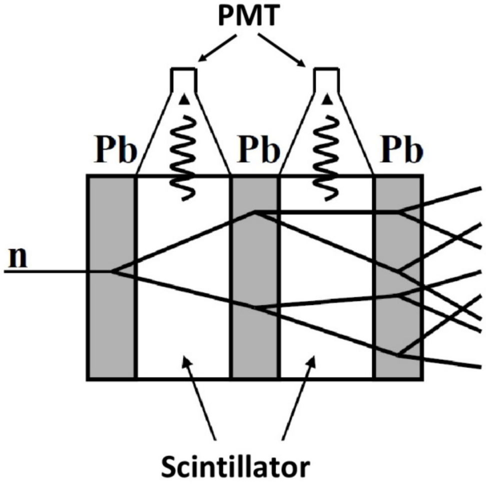

Figure 4.2: The principle of an hadronic calorimeter: alternating layers of absorbing and scintillating material cause the energy loss of the initial hadron and the scintillation light. This light is produced by secondary particles and detected by the PMTs. [7]

and absorbing material. When the hadron passes the absorber material, it looses energy via strong interactions. Secondary reaction products cause electromagnetic interactions in the scintillator that can be detected by the PMTs (see Fig. 4.2).

In *semiconductor detectors*, charged particles can create an electron-hole pair. These particles with inversed charge are separated by voltage. The ensuing electron flux can be measured, and by knowing the ionisation energy of the semiconductor the amount of energy loss per path length can be determined.

The *momentum* can be determined by the curvature a charged particle makes in a magnetic field. The momentum can be approximated with

$$p_\perp \approx 0.3 \cdot B \cdot R \left[\frac{\mathrm{GeV}/c}{\mathrm{Tm}}\right], \tag{4.2}$$

with R the radius of curvature and B the strength of the magnetic field. Here $p_\perp$ indicates the momentum component vertical to the magnetic field.

It is of utterly importance to detect the *trajectory* of a particle with high resolution, for example to determine the radius of curvature and hence the momentum. This can be done with time projection chambers (TPC), where the trajectory is directly visible. Other techniques use a sequence of measured

points as e.g. with wire chambers or strip detectors. Here thin wires or strips are arranged grid wise, in several layers and adjacent layers are oriented vertical to each other.
Neutrinos are in general not directly detectable. They might be identified by the energy or momentum deficit that can be calculated for a reaction, if the reaction is completely known otherwise.
[4, 5, 7, 18]

4.2 The CBM Detector

The CBM detector (CBM: **C**ompressed **B**aryonic **M**atter) is designed to explore the QCD phase diagram at moderate temperatures and high baryon densities. Its preparation is still in progress. CBM will be based at the future FAIR facility in Darmstadt/Germany. The CBM experiment is characterised in particular by the ability of precise measurements of particles with very low cross sections. This is realised by the high-intensity heavy ion beams that the future FAIR accelerator will supply and by the CBM detector that is capable making use of this rates. The detector is designed to record, trigger and analyze reaction rates up to 10 MHz [17]. This requires very fast and novel procedures to handle this enormous amount of data. In Fig. 4.3 a scheme of the CBM detector is shown. CBM will study the following topics in order to investigate the QCD phase diagram at high net-baryon densities: [19, p. 4-6]:

- Equation-of-state of baryonic matter at high densities.
- In-medium properties of hadrons.
- Phase transition from hadronic matter to quarkyonic or partonic matter at high net-baryon densities.
- Hypernuclei, strange di-baryons and massive strange objects.
- Charm production mechanisms, charm propagation and in-medium properties of charmed particles in (dense) nuclear matter.

These items will be explored for example by investigating phenomena like the collective flow of hadrons, the yields and mass distributions of particles, the decay chains of hypernuclei and other.
[17, 19]

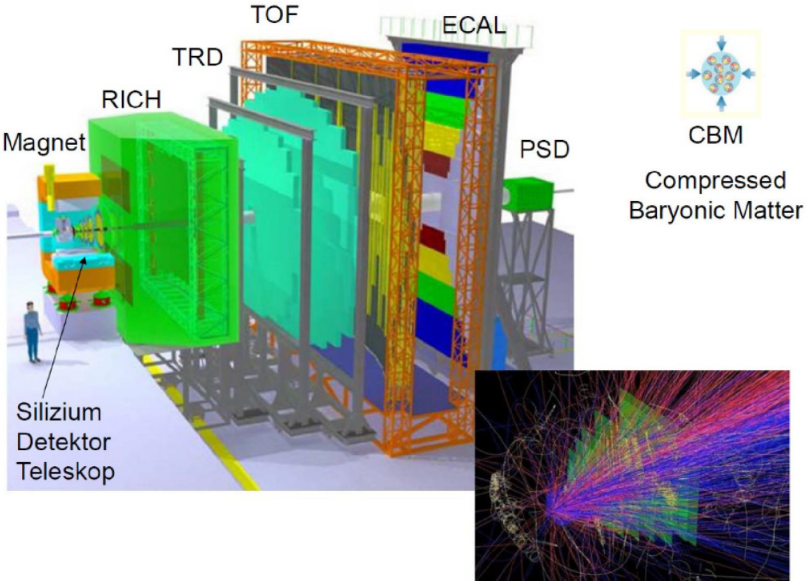

Figure 4.3: Scheme of the CBM detector, composed of its sub detectors (not all of them are listed). The beam from the left will hit the target that is in the region of the magnet. Since the CBM experiment is a fixed target experiment, the detector is build in forward direction from the collision point. The small image below shows simulated flight paths of the generated particles in central Au+Au collisions at FAIR. [7]

4.3 The CBM RICH Detector

4.3.1 Cherenkov Detectors

The CBM RICH (**R**ing **I**maging **Ch**erenkov) is a sub detector of the CBM detector and is designed to distinguish pions from electrons. Its detection principle is based on the Cherenkov effect that will be explained briefly in the following.

If a charged particle travels through a medium, the excited atoms emit photons. If the velocity v of that particle is higher than the velocity of light c' in this medium, the emitted photons form a cone (such as the Mach cone in acoustics). The opening angle of the cone depends on the particles velocity and hence its momentum and can be written as

$$\theta = \arccos\left(\frac{1}{n\beta}\right), \tag{4.3}$$

where $n = \frac{c_0}{c'}$ is the refraction index of the medium and $\beta = \frac{v}{c_0}$ as mentioned before. Since light is only emitted if $v > c'$, a threshold value for θ is given:

$$\cos\theta_c = \frac{1}{\beta n} < 1. \tag{4.4}$$

This is a great advantage, as it reduces the background noise of too slow particles.

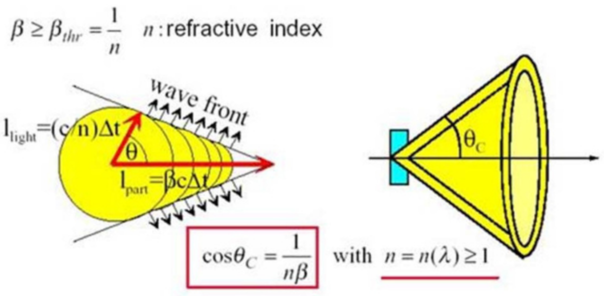

Figure 4.4: Cherenkov effect: A fast particle produces Cherenkov radiation that is emitted with the angle θ. Particles can be identified by the value of θ, and thus the ring radius that the focused cone shaped wave front leaves on the PMT plane. [7]

The Cherenkov effect is based on the particles velocity. By measuring the momentum p of a particle in the magnetic field and calculating its velocity via the opening angle θ, the mass of the particle can be determined. In practice, the angle θ is measured indirectly as diameter of the ring from the focused light cone on the PMT plane. So by displaying the ring diameter in dependence on the momentum, particles can be identified (see Fig. 4.5).
[5, 7, 19]

4.3.2 CBM RICH Detector

The principle setup of the CBM RICH detector is shown in Fig. 4.6. A particle beam hits the target and produces electrons amongst other particles. The electrons traverse the radiator gas and generate Cherenkov photons. These photons are reflected by the CBM RICH mirrors onto the photon detector plane that is made up of photo multipliers (PMTs). As radiator gas CO_2 is used with $n = 1.0045$ which will enable the detector to separate electrons from pions for momenta up to approximately 10 GeV. [19]

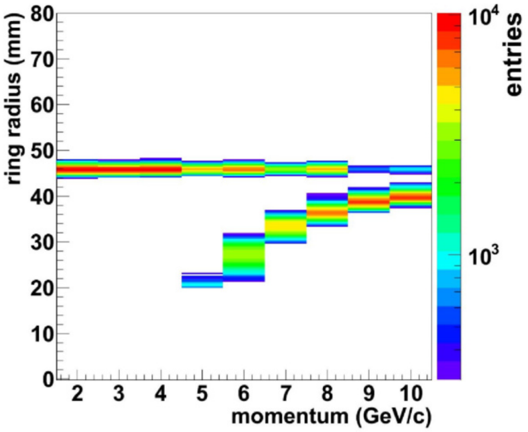

Figure 4.5: Dependence of the ring radius on the momentum of electrons (horizontal scale) and pions (lower branch). Below 4.7 GeV pions are too slow to produce Cherenkov radiation. In the range of 9-10 GeV the corresponding ring diameters of both particles are strongly approaching each other. Thus pions could be identified as electrons. [19]

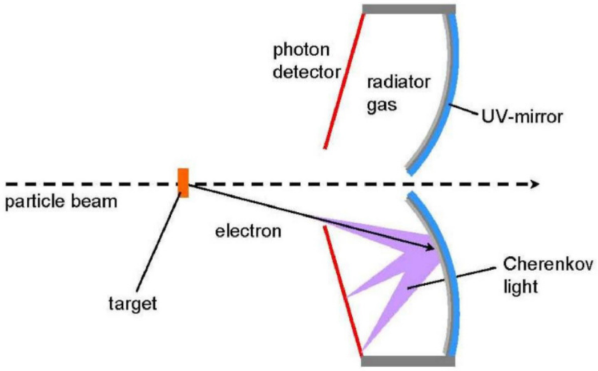

Figure 4.6: The principle setup of the RICH detector: the particle beam, coming from the left, hits the target and electrons are produced amongst other particles. They traverse the radiator gas and emit Cherenkov radiation. The light cone is reflected at the spherical mirror and thus focused as ring on the photon detector plane. [19]

4.3.3 RICH Mirrors

The CBM RICH detector has two spherical mirror planes that will reflect the photons onto the PMTs. Each one consisting of 40 (5 × 8) single squared mirrors with each 40 cm edge length and a radius of curvature of 300 cm. The photon yield is very small, about 20 photons will be measured per ring (see Fig. 4.7). Therefore it is of great importance to ensure that the mirrors will map the photons with very high accuracy onto the PMT plane. Several

methods exist to prove the image quality of mirrors, like reflectivity measurements, the D_0 test that proves the sharpness of the image, and the Ronchi test with which the geometry of the surface, more precisely its deviation from an ideal sphere, can be determined. The latter one is the main issue of this thesis and will be treated in detail in the following.
[19]

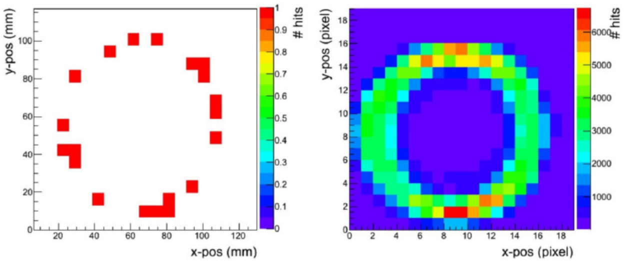

Figure 4.7: A single ring with 20 hits (left) and an integrated ring image (right), both generated by electrons at 6 GeV from a CBM RICH test beam experiment. [19]

5 Introduction into the Ronchi Test

The Ronchi test had been invented by Vasco Ronchi in 1923 to test the accuracy of the curvature of concave spherical mirrors. The principle is quite simple: Light, which comes from a point source that is located approximately at the mirrors center of curvature, is reflected by the mirror. The reflected light beam passes a grating of parallel lines with pitch P (a.k.a. Ronchi ruling) which is placed close to the point source (see Fig. 5.1). The image of the grating that is projected onto a detector is dependent on the precision of the mirrors spherical shape. If it is perfectly spherical, the projected lines will appear as straight as the lines of the grid. If it deviates from a perfectly spherical surface, the projected lines will be distorted, due to the mirrors surface, and hence their local pitch P_{loc} on the detector plane will vary. So by the shape of the lines, qualitative and even quantitative statements of the spherical shape can be made.

The test is only sensitive to changes of the radius of curvature that are perpendicular to the gratings direction. So to get entire information about the mirror surface, at least two measurements with different orientations (displaced by 90°) of the grating should be done.

There are two different concepts the Ronchi test can be performed: via geometrical optics or via wave optics. The first concept is done with course Ronchi rulings, where the distances between the lines are much greater than the wavelength λ of the light source, whereas the latter concept is performed with line distances of approximately the length of λ. Both types will be described below:

Using line distances of the order of λ, the interpretation of the measured pictures according to *wave optics* can be performed: The visible lines at the image point are an interference pattern, caused by diffraction of the light at the fine grating. To get a good resolution it is crucial to choose a grid with appropriate pitch P such that not more than two diffraction orders will overlap. The most convenient pitch depends on the wavelength λ and the numerical aperture $A_N = \frac{D/2}{f}$, where f is the focal length of the mirror and D its diameter (or edge length, respectively, for quadratic mirrors). With $A_N = \sin\theta_n$ (n being the nth diffraction order) and the above mentioned condition, that not more than two orders of diffraction should overlap, an

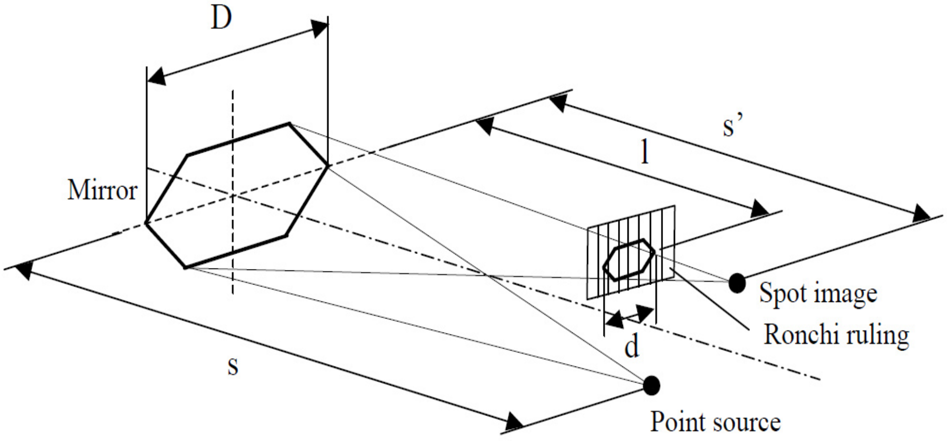

Figure 5.1: Principle setup of the Ronchi test. The detector is placed at the distance s' from the mirror, at the 'spot image' point. [20]

upper limit for P arises:

$$P \leq \frac{n\lambda}{A_N}. \tag{5.1}$$

Inserting the edge length $D = 400$ mm and focal length $f = 1500$ mm (values of the CBM RICH mirrors) one obtains

$$A_N = \frac{D/2}{f} = \frac{400/2}{1500} = 0.133 \Rightarrow P \leq \frac{n\lambda}{0.133}. \tag{5.2}$$

Since in this setup a white LED is used, λ is between 400 nm and 800 nm. So with $n = 1$ it follows:

$$\Rightarrow P_{lower} \leq 3\,\mu\text{m} \quad \text{and} \quad P_{upper} \leq 6\,\mu\text{m}.$$

Geometrical optics can be applied when using coarse Ronchi rulings. For the setup used for this thesis, this principle had been implemented with a grid with pitch $P = 200\,\mu\text{m}$.
With the nomenclature in Fig. 5.1 it can easily be seen that

$$\frac{d}{s' - l} = \frac{D}{s'} \tag{5.3}$$

and obviously the number of lines N_L seen at the image is $N_L = \frac{d}{P}$ (d and hence N_L can be adjusted via changing the distance between grid and detector).
With these relations and with the well-known mirror equation

$$\frac{1}{f} = \frac{2}{R} = \frac{1}{s} + \frac{1}{s'} \tag{5.4}$$

the radius R can be expressed as

$$R = \frac{2sDl}{s(D - PN_L) + Dl}. \tag{5.5}$$

With the last equations, for a mirror with locally varying radius it is possible to calculate the local radius R_{loc} by the local pitch P_{loc} of the grid image at the detector plane:

$$R_{loc} = \frac{2sP_{loc}l}{s(P_{loc} - P) + P_{loc}l}. \tag{5.6}$$

Here D had has been set equal to P_{loc} and $N_L = 1$ is used.
The implementation of the calculations in C++ is described in detail in chapter 7. The formulas used are more extensively than described in this section, but the underlying principle is the same, namely the calculation of the radius by the distance of neighbouring lines and distances of intersections of horizontal and vertical lines, respectively. [20][21]

6 Development of the Setup

6.1 Mechanics

To enable reliable and repeatable measurements, a solid mechanical setup had to be developed. The hardware of the setup consists basically of a light source, the Ronchi ruling, a detector (here: Andor iKon-M) with software (Andor SOLIS) to analyze the required data, and the mirror to test. For the illumination a light source module with an LED and a pinhole (see Fig. 6.1) had been developed by the universities mechanical engineer and produced by the workshop.

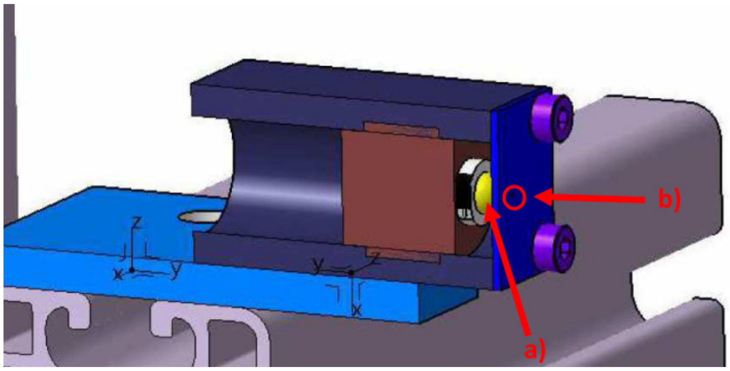

Figure 6.1: LED module (cross section), mounted on a rail. The distance between LED (a) and pinhole (b) is variable and the module is movable into all three dimensions.

The light source is approximately placed at the center of curvature (CoC) of the mirror, with a small vertical offset (≈ 55 mm) relative to the optical axis. The Ronchi ruling (RR) and the CCD camera are located behind the CoC, with the same offset (measured at the center of the CCD) from optical axis on the opposite side (see Fig. 6.2). All these components are mounted on a rail (see Fig. 6.3) and can be moved independently from each other.

As mentioned in chapter 5, the Ronchi test requires two consecutive shots of the Ronchi ruling between which the ruling will be rotated by 90°. Therefore a holder for the grid had been developed that allows the rotation without disassembling and displacing any other part.

The test mirror that had been used for the development of this setup is a prototype mirror for CBM RICH and is made up of glass. It is quadratic with an edge length of 40 cm, a thickness of 6 mm and a radius of 3 m. As

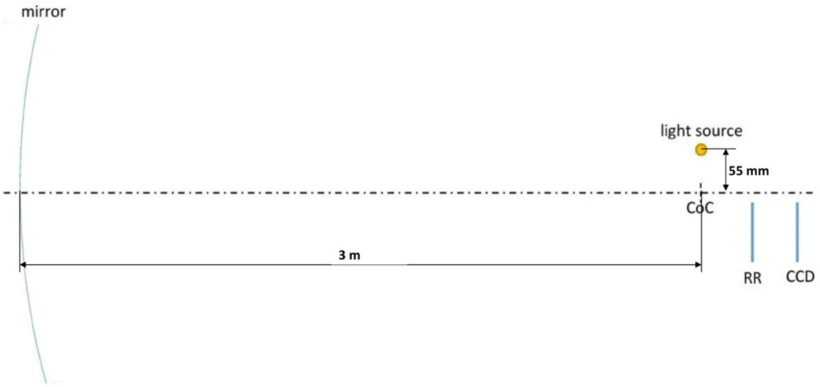

Figure 6.2: Schematic view of the setup with the locations of the mirror (left), its optical axis, center of curvature (CoC), light source, Ronchi ruling (RR) and CCD camera. At a distance of about 12 cm between CCD and CoC the Ronchigram image extends to the whole sensor.

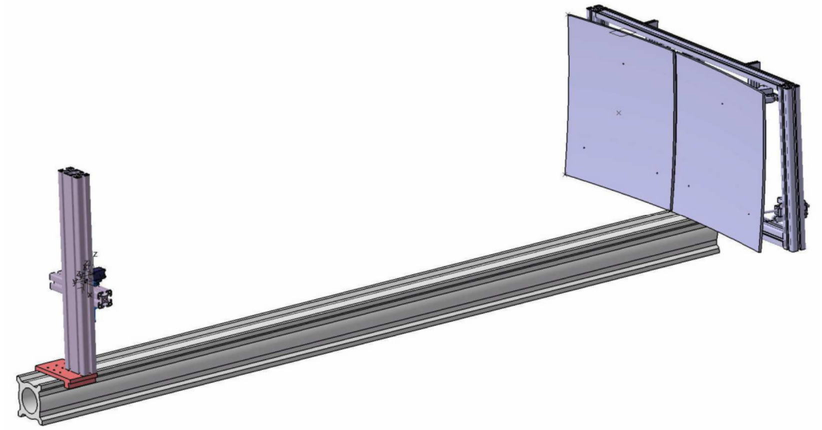

Figure 6.3: Overview of the setup: the light source module (without detector) on the left, mounted on posts and the mirror to test on the right. For this measurement only one mirror was placed centered to the optical axis.

reflective coating a thin aluminium layer is used at the front. An additional MgF_2 coating protects the aluminium layer [19].

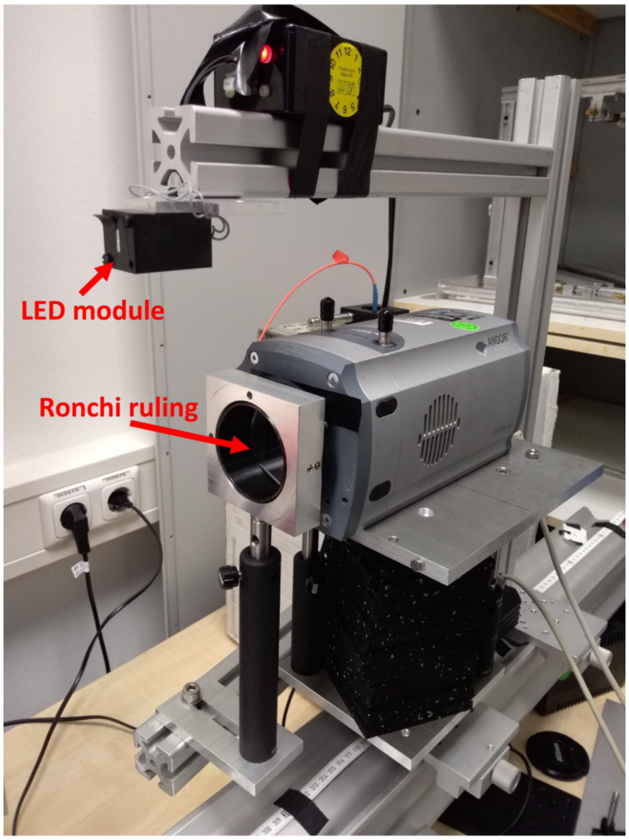

Figure 6.4: The complete measurement setup (without mirror).

A photograph of the setup is shown in Fig. 6.4.

6.2 Optimization of the Measurement

The first challenge setting up the Ronchi test was to get a clear image. The criteria for a good image are a uniform illumination, sufficient sharpness of the image and the minimization of stray light.

To reduce stray light and to keep the detector of overexposure, a black filter glass plate had been fixed in front of the CCD detector. Also, the curtain in the laboratory, surrounding the setup, had been closed when data were taken. Additionally, the window jalousies were closed to achieve as much darkness as possible. In Fig. 6.5 the difference of images taken with full darkness and

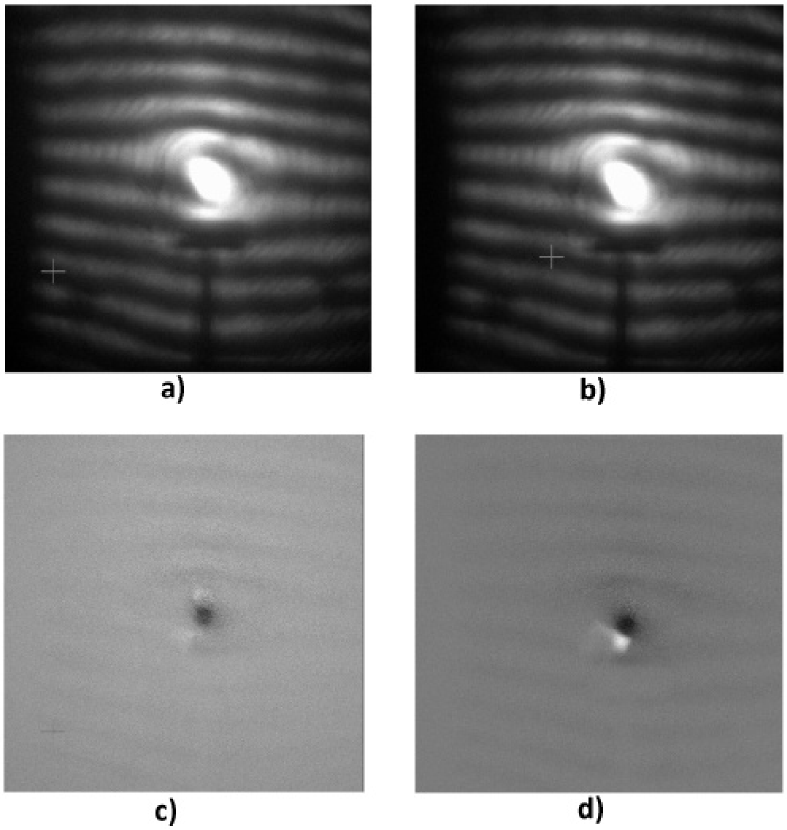

Figure 6.5: Investigating the effect of stray light: a): data taken in full darkness; b): data taken with open jalousies of the windows; c): difference a-b of both data; d): difference of two arbitrarily taken data with same conditions to ensure that their difference is close to the difference in c.

open jalousies, respectively, is shown. The result shows, that, as long as the curtain is closed, it makes nearly no difference if the jalousies are shut down or not, whereas closing the curtain is of particular importance. The contrast of the image increased with increasing exposure time. The default value is 0.02 seconds. With an exposure time of 0.5 seconds the background appears black instead of a noisy gray.

As known from the pinhole camera, the sharpness of a picture depends on the diameter of the pinhole. Since at first there was an ambiguity about the size of the pinhole diameter of the LED module, pinholes with diameters between 2.5 mm and 0.75 mm (which is the smallest the mechanical workshop

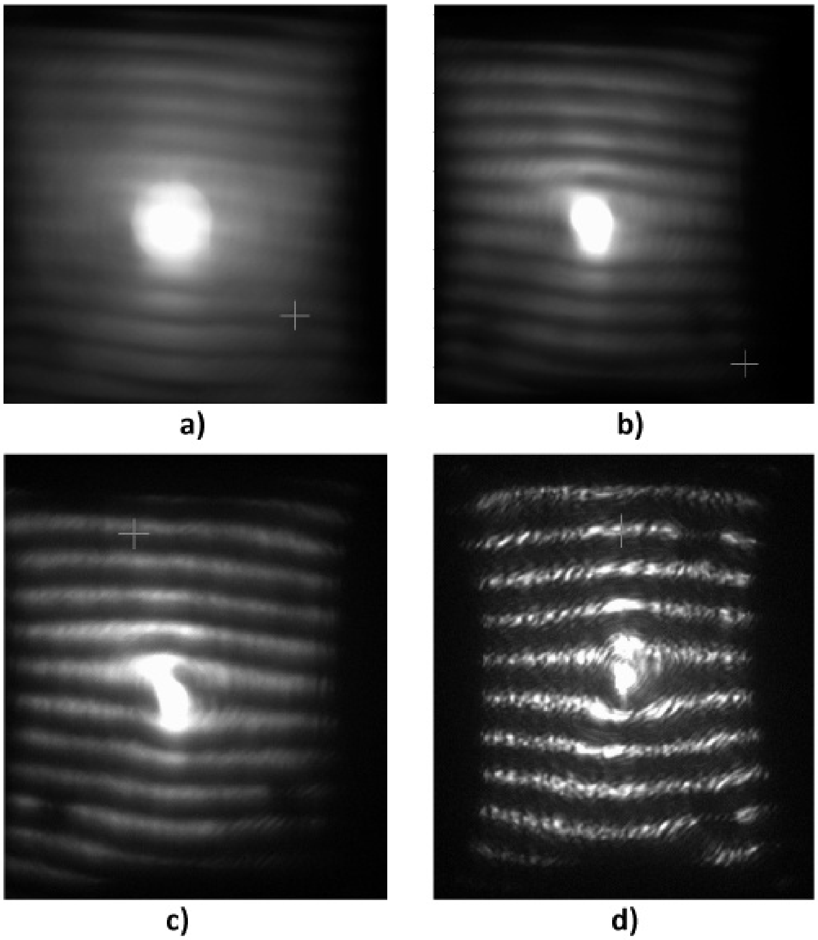

Figure 6.6: The effect of the pinhole diameter on the sharpness: From a) to d): pinholes of diameter 2.5 mm, 1.5 mm, 0.75 mm, 0.1 mm are used.

can fabricate) had been ordered. After a few tests it became obvious that with a pinhole diameter of 0.75 mm the image doesn't have enough sharpness yet, so further pinholes with 100 μm and 200 μm diameter had been ordered from Edmund Optics. With decreasing diameter the light becomes less, so more powerful LEDs were purchased to compensate. In Fig. 6.6 the effect of different pinhole diameters is seen. The image, taken with a 2.5 mm pinhole, appears very washy, with a 100 μm pinhole it has a good sharpness. Later measurements had been done with the 200 μm pinhole (with a diameter of

100 µm irregularities in the image disturbed further analysis).

Since the shape of the mirror is not a circle but quadratic, it is hard to get a uniform illumination all over the mirror, especially at the corners. Trying to vary the lateral distance of the LED module to the optical axis of the setup did not change anything. The illumination was influenced most by the distance between LED and pinhole. For the first measurements, the distance had been approximately 50 mm, after reducing this to about 5 mm, the corners were illuminated better (see Fig. 6.7).

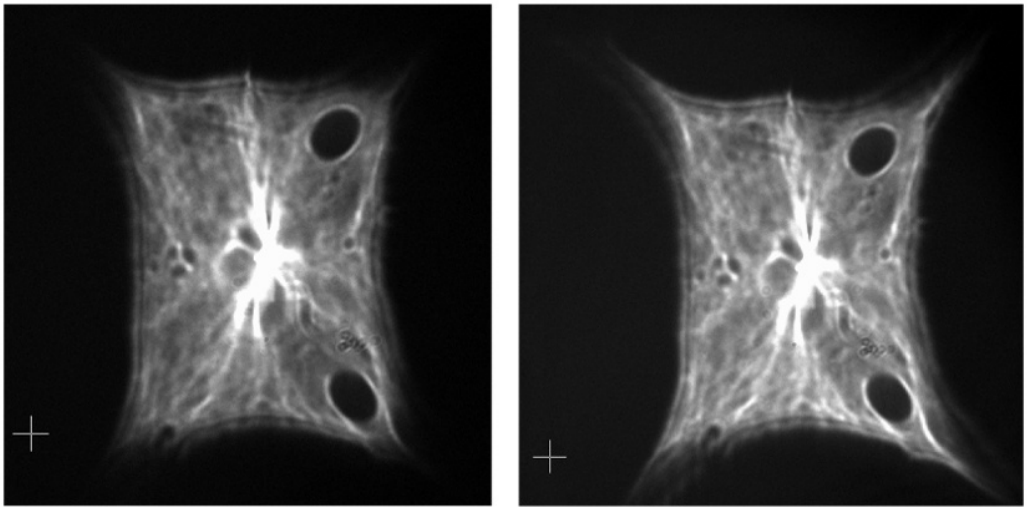

Figure 6.7: Effect of the distance between LED and pinhole on the illumination of the mirror: Left, the distance had been about 50 mm; Right image shows the illumination for an LED - pinhole distance of about 5 mm. Here the corners are illuminated significantly better.

A further question was, if the glass plate of the dark filter could influence the grid pattern. To investigate this, the pattern of two different orientations of the filter had been observed, but no differences were found.

The images of the mirror as shown in Fig. 6.7 show strong variations in the reflected light. One conjecture was that this is due to dust or irregularities on the surface of the optical components. To find the origin, pairs of data were taken and compared. In each pair either the LED, the filter or the mirror had been turned by 90°. In Fig. 6.8 the differences of all three data pairs are shown. Turning either the LED or the filter does not change anything. However, turning the mirror, the pattern turns as well. Thus, the stains

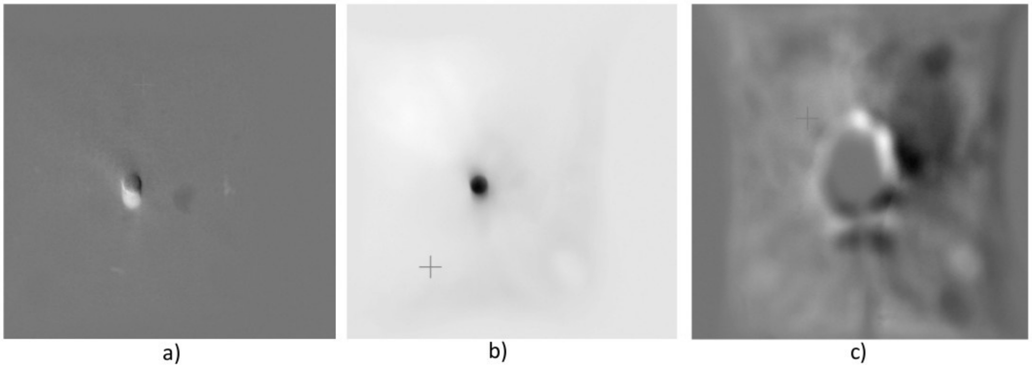

Figure 6.8: Differences of the three pairs of measurements between which the filter (a), the LED (b) and the mirror (c) had been turned by 90°. The first and second image are very smooth (except the dot in the middle), the third (c) data shows clear structures, indicating that the stains are caused by the mirror itself.

are caused by the mirror, maybe by dust or dirt on its surface. In future, measurements should be done with a new and clean mirror.
In all images taken, a bright spot appears in the middle of the mirror. This spot is a remnant of the spherical illumination of the mirror. In order to eliminate it, the center of the mirror can be shadowed with a round piece of cardboard. The best results had been achieved with a circle diameter of 70 mm.

As seen in Fig. 6.7 and 6.10, two black spots appear at the image. These spots are coming from distortions of the mirror surface that is caused by the mirror mountings on the back (see Fig. 6.9). Further investigation should be done on why only two of the three mountings cause the distortions and what can be done to avoid this.

6.3 Summary

Two typical images with vertical and horizontal oriented lines are shown in Fig. 6.10. The lines are slightly bowed outwards. This indicates that the surface is shallower than a sphere (if the sensor is located behind the center of curvature as it is in this setup). Summarized, best results of pictures for the Ronchi test were achieved with the following conditions:

- pinhole diameter: 200 µm

- exposure time: 0.5 seconds
- card board diameter: ≈ 70 mm
- distance LED - pinhole: 5 mm
- vertical offset of light source and CCD camera: ≈ 55 mm
- position of the CCD camera such that the mirror image fills almost the whole sensor
- distance of the front edge of the camera to the Ronchi ruling: ≈ 4 mm
- curtain closed, for dark environment

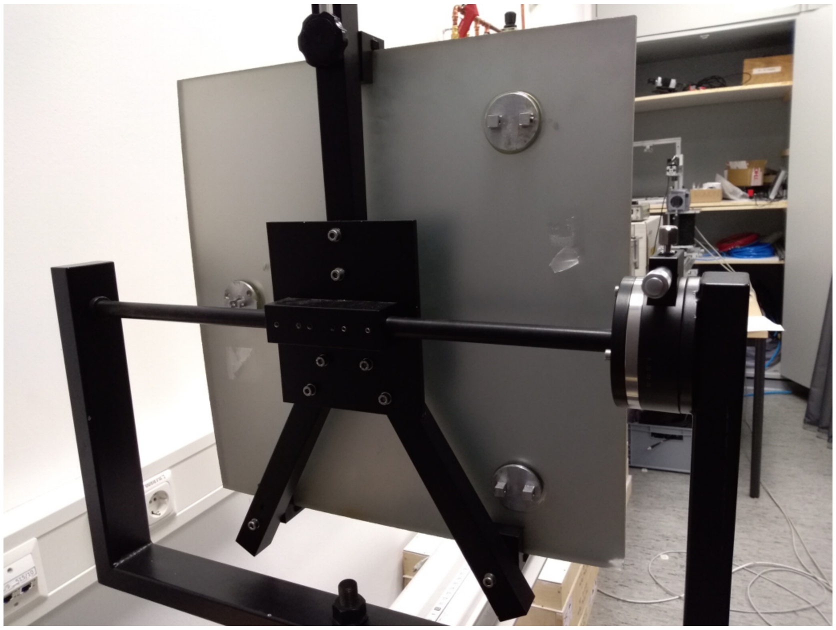

Figure 6.9: Back side of the mirror. Two of the three round mountings of the test mirror cause distortions on the front that lead to the black spots seen on the Ronchigrams.

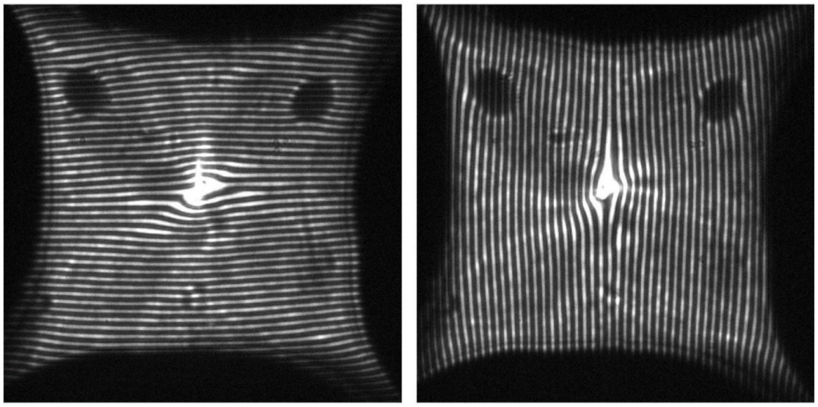

Figure 6.10: Two typical images with horizontal and vertical oriented grid. The lines are slightly bowed outwards. Using a setup, at which the CCD is placed behind the center of curvature, this indicates that the surface is shallower than that of an ideal sphere.

7 Implementation into C++

7.1 Overview

The Ronchi test can not only be used for a qualitative analysis as shown in chapter 6, but also for a quantitative evaluation of the local surface profile. The main analysis procedure for this quantitative approach is outlined in Fig. 7.1 and performed as described in Ref. [22]. At first the broad lines are turned into one dimensional lines (one pixel width), before both, the horizontal and vertical images, are superposed and the intersection points of the lines are extracted. Afterwards these intersections each are being assigned to a certain row and column number (indexed with i (column) and j (row)) to be able to express distances of intersections in terms of lines. Next, the mirror surface is split arithmetically into small plain segments, each one attached to a particular intersection point. Knowing their positions and measuring the positions and distances, respectively, of mirror, light source, ruling and CCD camera, the local normal of each segment can be extracted by calculating the slopes and angles of incident and reflected light beam. At this step, the center of each segment is considered to be in the tangent plane (see Fig. 7.2). Hence at first the arrangement of all segments describes a plane and not yet a spherical shape. Using the normals, the height differences (position

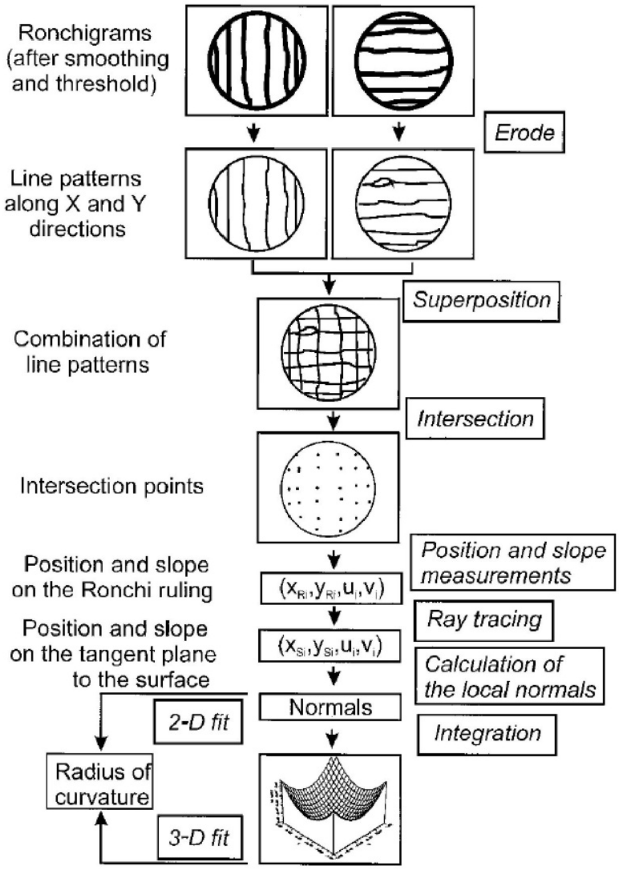

Figure 7.1: Outline of the calculation procedure, beginning with the raw image and ending with the calculated surface profile of the mirror. [22]

in z direction (z axis being the optical axis)) of the edges of neighbouring segments can be calculated. The final surface profile is obtained by, starting at the center of the image, varying the heights of the segments in such a way that the edges of neighbouring segments fit to each other. The inclination of the segments stays unchanged. In Fig. 6.10 two images (Ronchigrams) of a typical measurement were shown. Raw data like these are used for further analysis.

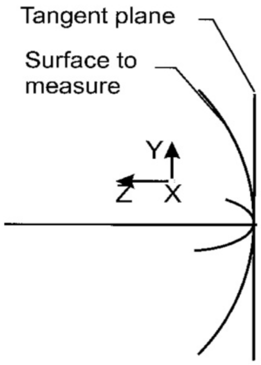

Figure 7.2: Tangent plane of the mirror. [22]

7.2 The Ronchi Test Algorithm

In the following, the C++ code, implemented for the quantitative Ronchi test analysis, will be described. The code consists of different functions which will be introduced consecutively. For orientation, the names of the corresponding functions are each included in the subtitles in typewriter script.
The images that will be analyzed are TIFF files and occur as `vector<vector<int>>` type in the code. Always when „image“ is being used in the following, this data type is meant.
The source code for the calculations has been submitted to the CBMROOT repository. The executive file is located in the folder
`aghoehne/soft/cbmroot_trunk/macro/rich/mirrors`
(file name: `run_ronchi.C`, revision number 15311), the source codes are placed in `aghoehne/soft/cbmroot_trunk/rich/mirrors`
(names: `CbmRichRonchiAna.cxx`, revision number 15311 and `CbmRichRonchiAna.h`, revision number 15311).

The coordinate system has been chosen as follows: The z axis is the optical axis of the mirror (see Fig. 7.2). When looking from the camera to the mirror, the x axis crosses horizontally and the y axis vertically. The origin of all three axes is defined at the center of the image on the CCD sensor.

7.2.1 Rotation of Vertical Image (`DoRotate`)

The procedure that had been established to process and calculate the Ronchigrams is coded for Ronchi images with horizontal lines. To avoid programming an extra code for vertical lines, images with vertical lines are transformed to images with horizontal lines by flipping the diagonally arranged corners. This is done before the data are processed further, and reversed by the same function (`DoRotate`) after the `DoLineSearch` procedure has been run.

7.2.2 Mean Intensity in y Direction (`DoMeanIntensityY`)

For better results in extracting the lines, this function scans the whole image and averages the brightness of a pixel with the brightness of several (here six per side) neighbouring pixels in y direction (i.e. perpendicular to horizontal lines). Therefore weighting values (multipliers) had been defined in descending order with increasing distance to the current pixel. These multipliers are set to be 160, 80, 40, 20, 10, 5.

Additionally, this function deletes the dark areas beyond the mirror contour to prevent searching for lines here and hence delivering false information (see Fig. 7.3). This is done by deleting pixels whose average intensity stays below a certain threshold (here 25).

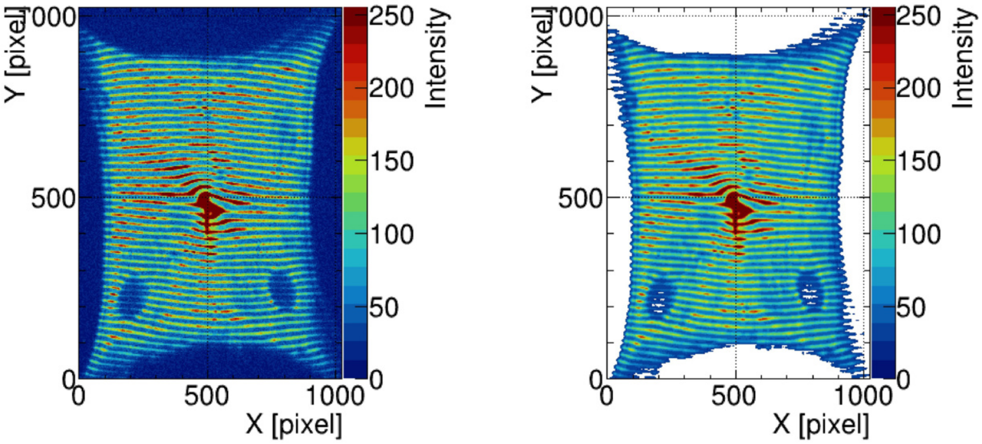

Figure 7.3: The image before (left) and after (right) averaging intensity in y direction and deleting dark areas.

7.2.3 Making the Lines One Dimensional (`DoPeakFinder`)

To be able to locate the intersection points very precisely, the broad lines are turned into lines with only one pixel width by extracting intensity peaks in

y direction. For this purpose the intensity of the current pixel is compared with the intensity of its n neighbours, whereas n depends on the grid pitch. Here n is chosen such that $2n \approx \frac{P}{2}$, where P is the pitch width in pixels ($P \approx 20$, pixel width: 13 μm). If an intensity peak is found, the data of this pixel (x and y position, intensity) is stored in a new image, while the remaining pixels are not considered anymore. The result is shown in Fig. 7.4.

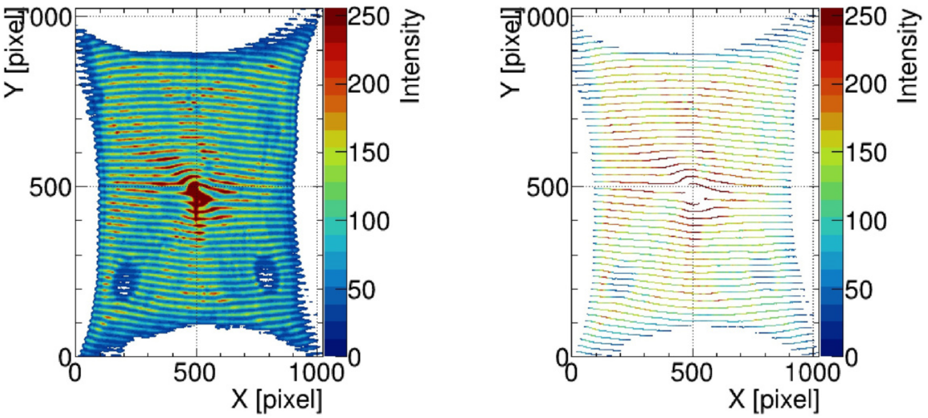

Figure 7.4: To determine an exact position of the lines, the broad bands are transformed into one dimensional lines.

7.2.4 Smoothing the Lines (`DoSmoothLines`)

Until now one dimensional lines have been achieved, but due to noise of the intensity in the original image the lines might appear serrate instead of smooth. To correct for this, the position in y direction of each line pixel has been averaged with the positions of its neighbours to the left and right side (see Fig. 7.5).

7.2.5 Indexing the Lines (`DoLineSearch`)

To be able to do proper calculations afterwards, it is necessary to index the intersections in columns and lines (i and j). Therefore the lines are indexed as follows:

First of all a variable `curIndex` is declared with value `Zero`. While scanning the image, each time a line is found this index is increased by `One` and the

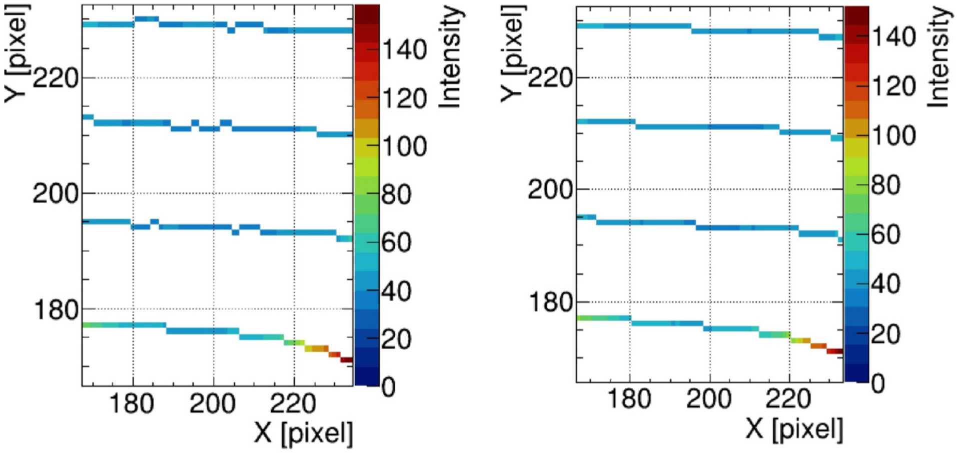

Figure 7.5: On the left and right side the same cut-out before (left) and after (right) application of the line smoothing procedure is shown.

corresponding line pixels are stored into a new image by a `FOR` loop that is searching for further pixels of the current line in x direction in a small range in y. The information of intensity is not necessary any more, hence only the index value is kept.

Since it might happen that some lines are not continuous but have gaps, a safety precaution breaks the loop if the gap is bigger than a certain threshold (60 pixels). This prohibits the possibility that the next found line is indexed with the current line index, although it might belong to the upper or lower row. This can happen since the lines are not absolutely horizontal but have slopes and the searching procedure is done in horizontal direction.

The images with vertical lines will be rotated after this procedure by the `DoRotation` function.

7.2.6 Extracting the Intersections (`DoIntersection`)

To extract the intersection points, the horizontal and vertical images are scanned simultaneously. Each time both have nonzero data at a given pixel, this position is stored with the corresponding line indices in a new created vector called `intersections`. In this vector also further data still to be calculated will be stored.

Due to the fact that the lines are not continuously straight but distorted, at some points two neighbouring line pixels of the same line are not in the same but adjacent row or column. Occasionally this happens with both the vertical

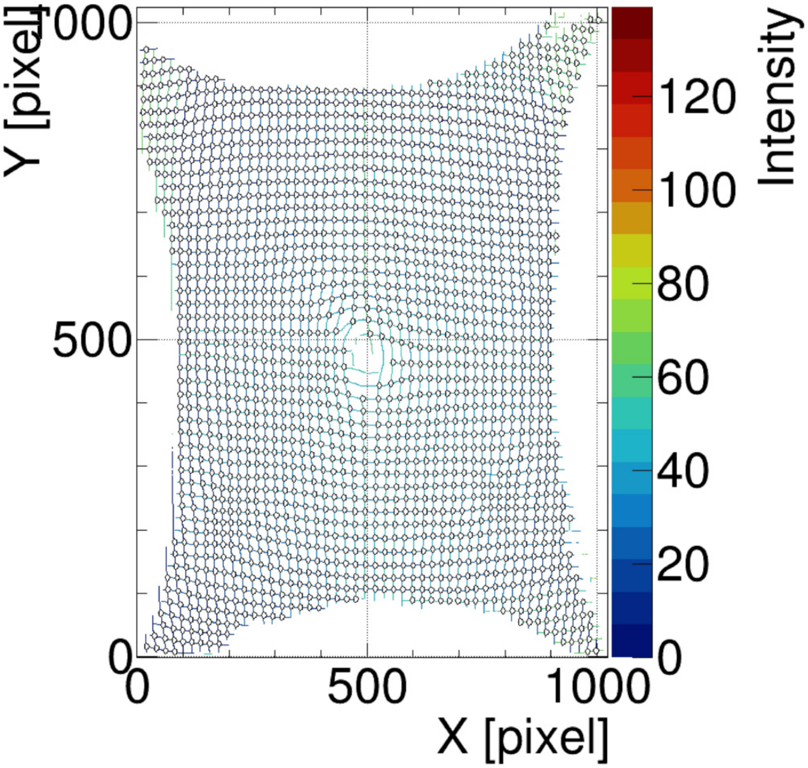

Figure 7.6: Superposition of the images with horizontal and vertical lines and the found intersections (circles). The x and y positions and indices of the intersections are the basis for further calculations.

and horizontal line at the same intersection point such that two neighbouring pixels have data from both images. The above mentioned procedure would identify this phenomena as two different intersection points instead of one. To avoid this, a subsequently implemented loop compares the distances of all intersections. If two of them are closer than a certain threshold (60% of average line distance), one of them will be deleted.
The following function `DoSuperpose` depicts the whole image, containing the grid and intersection points (see Fig. 7.6), but is not necessary for further calculations. It nevertheless is an important check of the routine.

7.2.7 Arranging the Lines (`DoOrderLines`)

Until now the lines had been indexed, but the previous procedure does not perfectly ensure that neighbouring lines have neighbouring indices. For later calculations it is crucial to express distances in terms of lines, therefore it is inevitable to number the lines in an ascending or descending order.
To order the lines, the `sort` function is used, together with `map`. At first a 4-tuple of data is stored for each intersection. The sorting is done by adding the x and y positions, respectively, of each pixel of each line. Dividing it by the number of pixels per line, one yields a mean value of the line, depending on the location of the line. Sorting the lines by these mean values arranges their indices in a correct order.

7.2.8 Calculating the Normals of the Segments (`DoLocalNormal`)

As mentioned in section 7.1, the mirror surface is split arithmetically into small segments whose total number is the number of intersections. The later construction of the sphere is based on the size and inclination of these segments. Their position on the mirror is defined by extrapolating the position of each intersection from the CCD camera to the mirror. Each extrapolated intersection defines the center of a segment. The size depends on the distance of the current intersection to its four direct neighbours (see Fig. 7.7) and hence is not necessarily equal to the size of the other segments.

For now, the center of each segment is considered to be at the tangent plane of the mirror so that initially they form a plane instead of a sphere (see Fig. 7.2). The inclination of a segment is expressed by the normal of its surface.

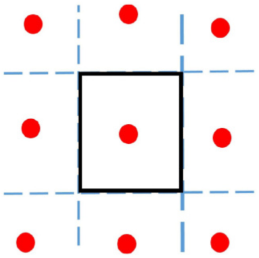

Figure 7.7: An arithmetical segment of the mirror (black frame). The blue dashed lines indicate the half distance between the current intersection and the neighbouring (not diagonal) intersections. Red dots are the extrapolated intersections.

These values are stored as a 2-tuple data set, containing the slopes in vertical and horizontal direction. These slopes are calculated from the slopes of the incident and reflected light beam.
The slope of the reflected beam in x/y direction is calculated by using the absolute height difference in x/y direction of the corresponding beam on the Ronchi ruling and the CCD sensor. This can be done since the pitch of the grid (200 μm) and the pixel size (13 μm) are known. For example (in y direction) if the considered intersection is located 10 lines, or 100 pixels, respectively, above the image center, the absolute height on the Ronchi ruling

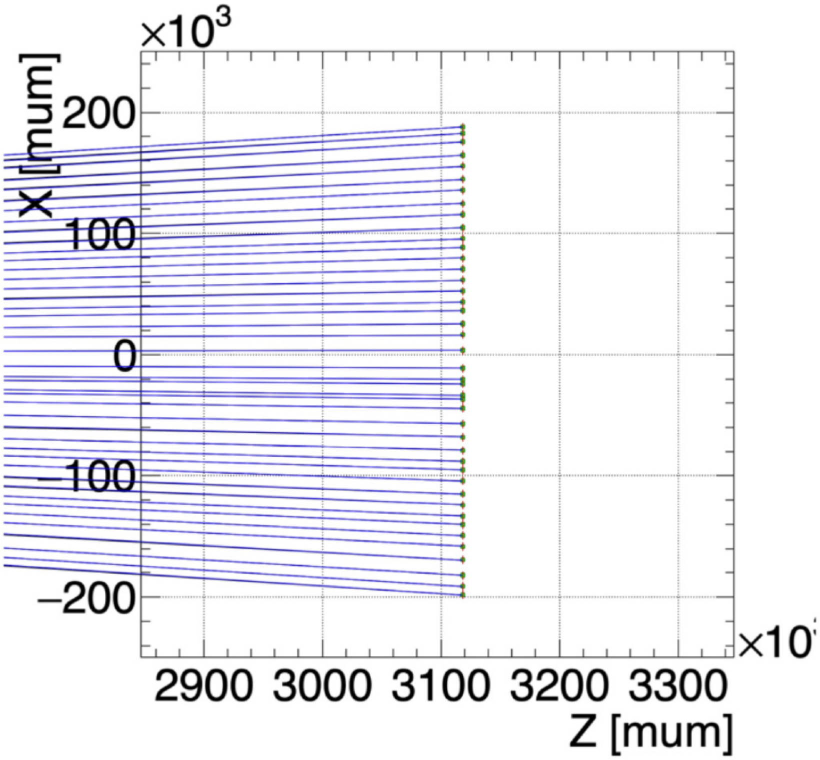

Figure 7.8: Reflected beams (blue), extrapolated from the CCD (not shown, located at $z = 0$) to the segments (dots at $\approx z = 3,120 \times 10^3$ μm), which are considered to be located at the tangent plane of the mirror. The slope of the extrapolated beams is calculated via the height difference of a detected beam (intersection) on the CCD and the Ronchi ruling. For more details see text.

is 10 x 200 µm = 2 mm whereas the absolute height on the CCD sensor is 100 x 13 µm = 1.3 mm. Knowing the slope and the position on the CCD, the impinging point of the incident beam onto the mirror is extrapolated by a linear function (see Fig. 7.8).

The slope of the incident beam can easily be calculated if the positions and distances of mirror, Ronchi ruling, CCD sensor, light source and impinging point of the light beam on the mirror are known.

To get the slopes of the normals, the slopes of the incident and reflected beam are converted into angles via trigonometrical functions. The angle ϑ_{normal_y} of a normal in y direction is calculated with $\vartheta_{normal_y} = \frac{\vartheta_{inc}+\vartheta_{ref}}{2}$, where the indices *inc* and *ref* are standing for incident and reflected beam. Afterwards the angles of this normal are being converted back to slopes and stored in the `intersections` vector.

7.2.9 Rotating the Segments and calculating new *x, y, z* positions `RotatePointImpl`

As described before, in the beginning the segment center are located at the tangent plane of the mirror. Since their normals in most cases are not parallel to the optical axis, the corners of the segments are not exactly in the tangent plane, but have an offset into z direction (see Fig. 7.9 a)). This so called height value depends on the inclination of the segment in x and y direction. To calculate the exact value, the principle of vector rotation had been used. Therefore for each segment four vectors have been defined that are pointing from the according intersection point on the CCD to the corners of the segments.

The change of the orientation of the segments and hence their z values can be described and calculated as consecutive rotations of these vectors around the z, y and x axis, if the axes are considered to be fixed [23]. The parameters of a rotated vector $\vec{V'}$ can be calculated from the initial vector $\vec{V}$ as follows:

$$\vec{V'} = R_z R_y R_x \vec{V}, \tag{7.1}$$

where R_x, R_y and R_z are the rotation matrices for rotations around the x, y and z axis. They are defined as

$$\begin{aligned} R_x &= \begin{pmatrix} 1 & 0 & 0 \\ 0 & \cos\vartheta_x & -\sin\vartheta_x \\ 0 & \sin\vartheta_x & \cos\vartheta_x \end{pmatrix}, \; R_y = \begin{pmatrix} \cos\vartheta_y & 0 & \sin\vartheta_y \\ 0 & 1 & 0 \\ -\sin\vartheta_y & 0 & \cos\vartheta_y \end{pmatrix}, \\ R_z &= \begin{pmatrix} \cos\vartheta_z & -\sin\vartheta_z & 0 \\ \sin\vartheta_z & \cos\vartheta_z & 0 \\ 0 & 0 & 1 \end{pmatrix}. \end{aligned} \tag{7.2}$$

The height values of the four edges and the center are stored in the `intersections` vector.

7.2.10 Constructing the Spherical Surface (`DoSphere`)

In order to construct a spherical surface from the segments, the individual segments have to be arranged in x, y and z directions. First, the segments are arranged in x and y such that their corners match. This procedure starts in the center. The distances of e.g. the two top left corners of two neighbouring segments are calculated and the segments placed next to each other. This procedure is run with all corners. Then the segments are arranged in z in order to construct the spherical surface: The distance in z direction of two directly adjacent corners is calculated and, again starting at the center, the segments are consecutively shifted on the z axis by this value (see Fig. 7.9) so that a more or less spherical surface is obtained.

7.3 Results and Discussion

In Fig. 7.10 an analysis of the test mirror is seen. The color scale indicates the deviation of the tested surface from an ideal sphere with a radius $R = 3$ m. Corresponding to this evaluation, the curve of the tested surface is a little bit deeper than that of an ideal sphere, up to -3 mm at the edges (the minus sign indicates a shape deeper than the ideal radius). As seen in Fig. 6.10, the bands of the grid are bowed slightly outwards. According to

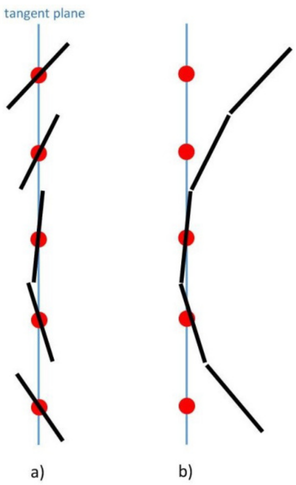

Figure 7.9: The sphere is constructed by calculating the initial height differences of neighbouring corners, when all segments are placed on the tangent plane (a), and then shifting the segments by the calculated difference, while keeping the orientation that is defined by the normal (b).

literature, if the ruling is placed behind the center of curvature (as it is in this setup), outwards bowed lines indicate that the surface curvature is shallower than a sphere [21]. This unfortunately contradicts our results. Thus further investigations have to be made to understand if an error exists in the calculations or distance measurements or elsewhere. The ideal radius value of the mirror had been varied in the calculations by ±10 cm, to see its influence on the results, but this did not have a significant impact. The deviation of the mirror surface from an ideal sphere varied between -1.5 mm and -4 mm at the edges [4].

At an earlier phase of the development of the code it happened that some lines were not continuous (after smoothing them to one dimension), but interrupted in between, such that no intersections could be detected there. For these cases a function had been implemented to interpolate the gaps linearly,

---

[4] These last values were roughly evaluated several weeks before the submission of this thesis. Due to the shutdown of the web page of the JLU Gießen after a serious IT security incident in December 2019, no further and more precise analysis could be done on the effect of varying the mirror radius (and other variables) on the results. This should be caught up later.

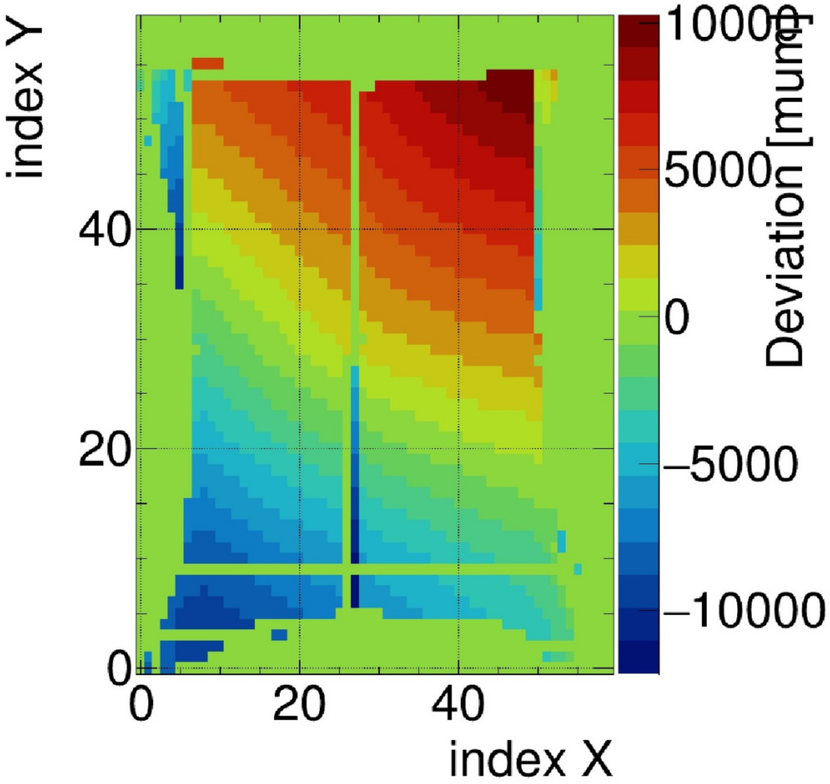

Figure 7.10: Evaluation of the test mirror: the various colors indicate the deviation of the mirror surface from an ideal sphere in μm. These values indicate a shape up to -3 mm deeper than an ideal sphere with $R = 3$ m. The areas that differ strongly from adjacent areas should be neglected for now.

if they are not too big (see older version of the code). After further improvement of the code this problem did not occur and the gap closing function had been deactivated.

Further some lines appear at areas, where there should not be one, e.g. between two regular lines. Therefore a procedure makes sure that intersections that are caused by these lines will not be considered in the calculations.

8 Discussion of Results

After the first phase of the project *qualitative* statements of the geometry of the mirror surface could be made. The Ronchigrams indicate that the shape of the mirror is slightly shallower than expected.
The quality of the image is disturbed by the bright spot in the center and the two dark spots on one side. In the area of the bright spot, no information about the position of the lines are given. A possibility to get results for this area could be to shield the CCD sensor by an additional black filter, so that the center would not be overexposed and to superimpose both, the image with the overexposed and the image with the properly exposed center. But this had not been tested yet. The dark spots are caused by the mountings on the back side of the mirror. At further developments it should be investigated why only two of the three mountings used cause this effect. However, information about the position of the lines is not lost at these areas.

To get *quantitative* statements of the mirror surface, a C++ calculation procedure had been developed. The analysis shows a shape that is deeper than an ideal sphere. The evaluated deviation is about -3 mm at the edges. This result contradicts the qualitative result from the first part and also the results from JLO Olomouc, where the mirror had been produced. Measurement results of that company give a deviation of the radius of +5 until +13 mm for the first four produced mirrors [19]. So further analysis should be done on the code and the setup to understand the discrepancies.

Main error sources are inaccuracies of distance measurements and the finite pixel size of the sensor. The larger distances, e.g. the distance between mirror and light source, are measured by a laser tracker whose precision is 1 mm. The accuracy of this measurement depends on accurate placing of the measuring device. The error therefor is estimated to be not more than 3 mm. The smaller distances are measured with a caliper, where possible, and with a measuring tape, respectively, with an error of about 2 mm.
The pixel size of the CCD camera of 13 μm limits the precision of the localization of the intersections on the CCD sensor to this value. On average, the distance of two intersections is about 20 pixels, so the uncertainty here is about 5% only.
Another systematic, but so far neglected error is the parallel shift of the light beams at the filter plate (in front of the sensor) and the Ronchi ruling.

Supposing a thickness of $d = 1.5$ mm of each glass plate and a refractive index of $n = 1.5$, at a maximum inclination of 3.8° (due to the mirror edge length of 40 cm and the distance of 3 m from the LED to the mirror), the shift can be calculated via Snell's law with a value of less than 0.04 mm per glass plate. In further development this shift should be considered in the calculations since it might be more effective as supposed in the beginning.

All in all this project had been a very successful step in developing a Ronchi test to measure the local surface homogeneity of the CBM RICH mirrors.
Attached is a short guidance for Ronchi tests at the CBM RICH mirrors.

Appendix

Instruction for acquiring Data

- Plug in Andor camera and LED.

- Start Andor SOLIS software. Settings:
  · Exposure time: 0.5 seconds (increases contrast compared to default setting of 0.02 seconds);
  · Image: vertically flipped (optional, not necessary)

- Positions of devices:
  · LED module: in direction of optical axis it has to be at the center of curvature (CoC) and shifted by approx 57 mm in y direction (vertical) above optical axis.
  · Camera: behind the LED module, outside of the CoC. Choose the distance so far that the image fills the whole CCD sensor. The center of the CCD has to be approx. 58 mm below the optical axis in y direction.
  · Adjust the mirror by the adjusting screws, to direct the reflected light into the detector
  · Ronchi ruling: directly in front of the camera, such that the line distances are similar to the presented images in this thesis.

- Acquire data (with vertical and horizontal orientation of the Ronchi ruling) and save it as TIFF file with the mirrors identification number.

- Measure and note all relevant distances:
  · Mirror - LED
  · Mirror - CCD
  · CCD - Ronchi ruling
  · Offsets of each LED and CCD to optical axis (in x, y and z).

- Enter the measured distances in the code.

- Run the calculations.

Acknowledgements

At this point I would like give thanks to Prof. Dr. Claudia Höhne who accompanied my project and always was willing and motivated to help with problems.
Furthermore I want to thank my supervisor Dr. Semen Lebedev who was a great help in developing the code for the measurements and patiently explained things that were unintelligible to me.
A great thank-you also to my dear wife who encouraged me to study physics and to stay in physics and supports me as much as she can.
And finally I am thankful to God for helping me with my studies and especially with this thesis.

References

[1] Hans J. Störig: *Kleine Weltgeschichte der Philosophie*; S. Fischer Verlag GmbH, Frankfurt 1999, 4th edition

[2] John Lennox: *Gunning for God*; Lion Hudson plc Oxford, England 2011, 2nd edition

[3] David J. Griffiths: *Introduction to Quantum Mechanics*; Pearson Education, Upper Saddle River 2005, 2nd edition

[4] B. Povh, K. Rith, C. Scholz, F. Zetsche, W. Rodejohann: *Teilchen und Kerne*; Springer-Verlag Berlin Heidelberg 2014, 9th edition

[5] Jörn Bleck-Neuhaus: *Elementare Teilchen*; Springer-Verlag Berlin Heidelberg 2013, 2nd edition

[6] `https://www.weltderphysik.de/gebiet/teilchen/experimente/streuversuche/geschichte-der-streuversuche/` (called 2019/08/16)

[7] *Particle Physics* lecture of Prof. Dr. Claudia Hoehne; winter semester 14/15

[8] `https://home.cern/science/physics/standard-model` (called 2019/08/22)

[9] T. Morii, C. S. Lim, S. N. Mukherjee: *The Physics of the Standard Model and Beyond*; World Scientific Publishing Co. Pte. Ltd. 2004

[10] *Particle Physics Booklet*; PDG 2018

[11] `https://www.abc.net.au/news/science/2017-07-15/the-standard-model-of-particle-physics-explained/7670338` (called 2019/08/22)

[12] `https://home.cern/news/news/experiments/lhcb-confirms-existence-exotic-hadrons` (called 2019/08/22)

[13] `https://fair-center.eu/for-users/experiments/nuclear-matter-physics/cbm/introduction.html` (called 2019/09/05)

[14] S. Sarkar, H. Satz, B. Sinha: *The Physics of the Quark-Gluon Plasma*; Springer-Verlag Berlin Heidelberg 2010

[15] Prof. Dr. K. Reygers, Prof. Dr. J. Stachel, Physikalisches Institut, Universität Heidelberg, SS 2015: `https://www.physi.uni-heidelberg.de/~reygers/lectures/2015/qgp/qgp2015_03_thermo.pdf`

[16] Prof. Dr. Christian S. Fischer: *QCD at finite temperature and chemical potential from Dyson-Schwinger equations*; paper; January 2019

[17] CBM Flyer from FAIR Webpage

[18] `https://www.weltderphysik.de/gebiet/teilchen/experimente/teilchenbeschleuniger/lhc/lhc-experimente/atlas/atlas-detektor/` (called 2019/09/05)

[19] Technical Design Report for the CBM RICH detector, June 2013

[20] Dissertation of Martin Laub: *Development of opto-mechanical tools and procedures for the new generation of RICH-detectors at CERN*; 2001

[21] PDF file of John Nichol: *The Ronchi Test*; downloaded at `https://nicholoptical.files.wordpress.com/2016/11/the-ronchi-test.pdf`

[22] Paper of Santiago Royo, Josep Arasa, and Carles Pizarro: *Profilometry of toroidal surfaces with an improved Ronchi test*; ©2000 Optical Society of America; 1 November 2000 / Vol. 39, No. 31 / APPLIED OPTICS

[23] Thomas Luhmann, Stuart Robson, Stephen Kyle, Jan Boehm: *Close-Range Photogrammetry and 3D Imaging*; Hubert & Co. GmbH & Co. KG, Göttingen 2014

Selbstständigkeitserklärung

Hiermit versichere ich, die vorgelegte Thesis selbstständig und ohne unerlaubte fremde Hilfe und nur mit den Hilfen angefertigt zu haben, die ich in der Thesis angegeben habe. Alle Textstellen, die wörtlich oder sinngemäß aus veröffentlichten Schriften entnommen sind, und alle Angaben die auf mündlichen Auskünften beruhen, sind als solche kenntlich gemacht. Bei den von mir durchgeführten und in der Thesis erwähnten Untersuchungen habe ich die Grundsätze guter wissenschaftlicher Praxis, wie sie in der ‚Satzung der Justus-Liebig-Universität zur Sicherung guter wissenschaftlicher Praxis‘ niedergelegt sind, eingehalten. Gemäß § 25 Abs. 6 der Allgemeinen Bestimmungen für modularisierte Studiengänge dulde ich eine Überprüfung der Thesis mittels Anti-Plagiatssoftware.

Unterschrift, Ort, Datum